

Cosmic strings, domain walls and environment-dependent clustering

Øyvind Christiansen,^{1a} Julian Adamek^{b,c,d} and Martin Kunz^d

^aCEICO, Institute of Physics of the Czech Academy of Sciences
Na Slovance 1999/2, 182 00, Prague 8, Czechia

^bInstitut für Astrophysik, Universität Zürich
Winterthurerstrasse 190, 8057 Zürich, Switzerland

^cInstitut für Teilchen- und Astrophysik, ETH Zürich
Wolfgang-Pauli-Strasse 27, 8093 Zürich, Switzerland

^dDépartement de Physique Théorique, Université de Genève
24 quai Ernest-Ansermet, 1211 Genève 4, Switzerland

E-mail: oyvinch@fzu.cz, adamekj@ethz.ch, martin.kunz@unige.ch

Abstract. Recent cosmological data favour phantom-crossing dark energy, motivating models with non-minimal couplings that induce a fifth force on structure formation. Reconciling these models with local tests often requires strong screening, leading to environment-dependent clustering. We investigate such effects via a late-time structure-induced phase transition driven by a non-minimally coupled scalar field. For this purpose, we introduce `norns`, a fully relativistic cosmological particle-mesh code that self-consistently evolves a complex scalar field – a generalisation of the symmetron producing global $U(1)$ strings rather than domain walls. Using simulations, we compare string and wall-forming models, quantifying impacts on the matter power spectrum, halo mass function, and defect dynamics. Strong environment-dependent effects can generate significant departures from Λ CDM in underdense regions while keeping the overall power spectrum changes modest ($\sim 4\text{-}15\%$ at $k \sim 0.3\text{-}0.5 h \text{ Mpc}^{-1}$, sub-percent for $z \gtrsim 0.2$). We find that an attractive fifth force can locally suppress structure growth in voids while enhancing it in surrounding overdense regions by driving outflows from the voids. These effects leave distinctive signatures in the matter density probability density function and in marked halo power spectra, which are likely detectable in low-redshift data.

¹Corresponding author.

Contents

1	Introduction	1
2	Method	3
2.1	Model	3
2.2	Defect finding	4
2.3	Parameter choices	5
3	Results	7
3.1	Density distribution	11
3.2	Probes of environment-dependent effects	16
4	Summary and conclusion	22
A	String profile	27
B	Convergence	28
C	Performance	30

1 Introduction

The standard model of cosmology, Λ CDM, asserts that 95% of the energy content of the late-time Universe resides in a *dark* sector, consisting of a cosmological constant energy density, ρ_Λ , and cold dark matter (CDM). Their phenomenology is purely gravitational and explains the late-time accelerated expansion of space and observed features of gravitational structures and clustering. While the cosmological constant is especially poorly understood [1, 2], progress on cold dark matter has historically been expected from particle accelerator experiments such as ATLAS and CMS, probing promising candidates within the framework of, for example, supersymmetry [3]. The lack of observations of effects from the dark sector on standard-model particles motivates a continued study into dark sector alternatives for model comparison and application to reported cosmological and astrophysical tensions.

An interesting family of extended dark sector models introduces a phase transition in late-time cosmology. This has been shown to allow some improvement in joint analyses of cosmic microwave background (CMB) and large-scale structure (LSS) data [4–6], and has also been studied in astrophysical contexts [7–9]. A particular relativistic realisation of such a model is the symmetron [10, 11], where an additional scalar field ϕ has a universal and non-minimal coupling to the stress energy of the matter sector. In the limit of small field excursions, the symmetron potential can be thought of as a Taylor polynomial and representative of a greater subset of the Horndeski theory landscape, encompassing models such as Brans-Dicke or dilatons which generically appear in the low-energy limit of string theory [12]. The phase transition of the symmetron is controlled by the ambient stress energy of the matter fluid that maintains the symmetron’s \mathbb{Z}_2 symmetry in overdense environments; therefore, the model can in principle comply with strict astrophysical constraints in the local neighbourhood [13–15]. An indication for a *phantom crossing* has recently been reported in the dark energy equation of state parameter [16–18], for which, among others, non-minimally

coupled models have been studied [19–21], and the symmetron model in particular in [22]. If the symmetron undergoes its phase transition at redshifts relevant for dynamical dark energy, around $z \sim 0.6$, then the small energy scale associated with the critical ambient density, ρ_* , implies that the field must undergo large field excursions to reach an energy scale comparable to dark energy. This in turn produces very strong fifth forces, which must be countered by correspondingly strong screening effects. The Structure-Induced Phase Transition (SIPT), found in [23] and discussed below, is especially interesting in this context. SIPT-type models may be applied to address the coincidence problem of dark energy, by relating a late-time phase transition to nonlinear structure formation. As such, it can be seen as an extension on back-reaction models, that have been shown to not work in standard Λ CDM (e.g. [24]). As we will see in Section 2, reaching energy-scales relevant to dark energy in the SIPT-regime of the parameter space requires a generalisation of the symmetron model, by e.g. introducing non-perturbative conformal factors or potentials.

The symmetron adds a single additional scalar field, $\phi \in \mathbb{R}^1$, where a spontaneously broken \mathbb{Z}_2 symmetry results in the formation of domain walls between two degenerate vacua. By choosing the field to be complex, $\phi \in \mathbb{C}^1$, it breaks a global $U(1)$ symmetry, resulting in string defects forming at the locations of phase discontinuities. The respective defects can be formed by the Kibble mechanism [25] or as a result of phase transitions occurring independently in different underdense patches of the Universe – the case of SIPT. One can similarly produce monopoles or textures by promoting the scalar field to a 3- or 4-vector, respectively. For more information on the application of topological defects in cosmology, we direct the reader to the useful reviews [25–29]. Recently, in [30], the complex symmetron was considered in a simple ideal scenario to study the ability of overdensities to pin and stabilise strings, as has been shown for the case of domain walls in [31].

Here, for the first time, we perform cosmological simulations of non-minimally coupled cosmic strings in the late-time Universe, and show side by side comparisons to the domain-wall scenario of the real-valued symmetron field. We demonstrate differences in their effects on matter clustering, dark-matter halo statistics, defect dynamics, and their pinning to overdensities. We provide estimates of fifth-force effects on dark-matter halos, particle and halo velocity dispersions, and discuss target observables for constraining the model in upcoming experiments. In particular, we demonstrate strong signals in the matter density probability function and in marked statistics, and discuss them in relation to ongoing galaxy surveys. We provide visualisations of the simulation data in interactive figures and animations.¹

The simulation code was developed based on the scheme of **ISIS** [32–34] in which the real-valued symmetron is simulated on a lattice on top of the Newtonian N-body code **RAMSES** [35]. In **asevolution** [23, 36], this method was implemented in the fully relativistic weak-field particle-mesh code **gevolution** [37–40], which allows to consistently treat dark sector energy transfer, back-reaction effects and relativistic particle velocities. It was additionally extended to evolve gravitational waves in **AsGRD** [41]. Large scalar masses $\mu \gg (D/1\text{ m}) \times 0.1 \text{ neV}$, can be constrained in laboratory experiments [42], where D is the scale of the experimental setup, while cosmologically relevant Compton wavelengths, L_C , are constrained by solar system and galactic observations [10]. In [23], the SIPT-regime of the symmetron parameter space was explored that allows for inhomogeneous phase transitions within underdense voids. This part of the parameter space presents interesting and novel phenomenology, is relatively poorly constrained as the usual modelling does not apply – see e.g. figure 5 of [43] for $\rho_{\text{SSB}} < \bar{\rho}$ –

¹<https://www.oyvindchristiansen.com/projects/rcsymmetron>

and will be the target for this work as well.

The simulation code `norns` (NOn-linear and Relativistic Numerical Strings) is made publicly available,² while the evolution of the real-valued symmetron is done with `AsGRD`.³ Convergence and resolution tests, as well as code performance are discussed in appendices A–C. In addition to evolving the symmetron, the simulation codes present a simple and rigorous framework for the inclusion of physics beyond the standard model into nonlinear structure formation. In the past, `gevolution` has also been applied, for example, to k -essence and KGB dark energy and $f(R)$ gravity [44–46].

2 Method

The implementation scheme generally matches that presented in [23, 36], but with the exception of the promotion of the symmetron to complex-valued $\phi \in \mathbb{C}$. We give a short overview of the new methodological aspects here, while the reader is directed to the references for the remainder of the treatment. We detail the post-processing methodology for the statistics that we present together with the results in Section 3.

2.1 Model

The symmetron model is formulated in the Einstein frame with a Klein-Gordon plus a self-interaction potential. The metrics of the Einstein and Jordan frames, $g_{\mu\nu}$ and $\tilde{g}_{\mu\nu}$, respectively, are related by a conformal transformation as $\tilde{g}_{\mu\nu} = A^2(\phi)g_{\mu\nu}$. In the Jordan frame, the scalar is uncoupled to the matter sector but achieves a universal matter coupling on transformation to the Einstein frame. The matter Lagrangian is written in the Jordan frame and is $\mathcal{L}_m(\tilde{g}_{\mu\nu}, \Psi_i)$, for the standard model fields Ψ_i . On varying with respect to ϕ , it generates a term $-\frac{A_\phi}{A}T_m$, where T_m is the trace of the stress energy of the Einstein frame matter sector and is equal to the negative of the matter energy density $T_m \approx -\rho_m$ in the nonrelativistic limit. This allows us to write an effective potential from which the equations of motion are easily obtained,

$$V_{\text{eff}}(\phi) = -\frac{1}{2}\mu^2\phi^\dagger\phi + \frac{\lambda}{4}\left(\phi^\dagger\phi\right)^2 - T_m \ln(A[\phi]). \quad (2.1)$$

We consider both cases $\phi \in \mathbb{C}, \mathbb{R}$. Now, the full effective Lagrangian density for the symmetron is given by

$$\mathcal{L} = -\frac{1}{2}(\partial_\mu\phi)^\dagger(\partial^\mu\phi) - V_{\text{eff}}(\phi). \quad (2.2)$$

We also define

$$V_0 \equiv \frac{\lambda}{4}v_0^4 = \frac{9\Omega_{m,0}^2H_0^2}{2a_*^3}\frac{\beta^2\xi_*^2}{a_*^3} = \frac{9\Omega_{m,0}^2H_0^2}{2a_*^3}\Delta A_{\text{max}}, \quad (2.3)$$

$$dA \equiv A - 1 = \frac{1}{2}\left(\frac{\phi}{M}\right)^2 \lesssim \frac{\beta^2\xi_*^2}{a_*^3}, \quad (2.4)$$

where V_0 is the energy difference between the false vacuum ($\phi = 0$) and the true vacua ($\phi = \pm v_0$), and we have Taylor expanded the potential $V(\phi)$ and the conformal factor $A(\phi)$,

²The code will be made available after peer-review.

³<https://github.com/oyvach/AsGRD>

assuming \mathbb{Z}_2 symmetry on $\phi \rightarrow -\phi$, and small field excursions $dA, |\phi/M_{\text{pl}}| \ll 1$, where M_{pl} is the Planck mass. $\Delta A_{\text{max}} = \beta^2 \xi_*^2 / a_*^3$ is the deviation of the conformal factor from unity in the true vacuum (where $T_m = 0$).

The model has three free parameters: the bare tachyonic mass μ , the self-interaction strength λ and the conformal coupling M . These are analogous to the phenomenologically related quantities of the Compton wavelength compared to the current time Hubble length $\xi_* \equiv L_C H_0$, the scale factor of the phase transition in a homogeneous universe $a_* = 1/(1+z_*)$ and the fifth force strength relative to the Newtonian gravitational force for small perturbations around the true vacuum $F_5/F_N \simeq 2\beta^2$. They are explained in more detail in [36, 47].

From Eq. (2.3), we observe that if we require $\Delta A \lesssim 0.1$ to remain in the perturbative regime, which currently is a limitation of our weak-field expanded scheme [36, 38], we have

$$\frac{V_0}{\rho_{c,0}} \sim 1.5 \times 10^{-2} \left(\frac{\Delta A}{0.1} \right) a_*^{-3}. \quad (2.5)$$

This means that we cannot have a significant effect on the background in the perturbative ΔA regime for the interesting case of SIPT⁴ that is also accessible to our simulations. The background evolution therefore remains well approximated by ΛCDM in this case. However, we note that the Universe is significantly more inhomogeneous at early redshifts for smaller smoothing scales $L_C \ll 1 \text{ Mpc}$, which is expected to allow for the SIPT type of phase transition at smaller a_* . Some of the phenomenology explored here might also be taken as representative for this regime. Treating non-perturbative ΔA is beyond the scope of the current work and requires a generalisation of the particle geodesic solver [36]. For steeper barriers, for example, when the bounding potential term contains ϕ^N , $N > 4$, one can have a larger V_0 while keeping v_0 and thus $dA(v_0)$ (also $\beta \sim v/M^2$) small. With a sine-Gordon potential in particular $V \supset \mu^2(1 - \cos(\phi/f))/2$, the minimum and amplitude can be set separately, and therefore allow large energy contents in the symmetron sector while keeping conformal factors perturbative and fifth forces either large or small. Such potentials have particular relevance for axion dark matter models [48], and will be the subject of a future project. For now, we keep the symmetron potential at quartic order, and use it as a proxy for studying environment-dependent signatures representing a broader class of SIPT-models with different potentials, conformal factors, kinetic structure, non-universal couplings or multiple fields.

2.2 Defect finding

In order to identify strings in the simulations, we follow the procedure laid out in [27], see Fig. 1. If a string passes through a region, then the closed line integral along a path enclosing the string will give the string's ‘winding number’ N

$$N = \frac{1}{2\pi} \oint d\varphi, \quad (2.6)$$

where φ is the complex phase. Therefore, an indication that the region enclosed contains a string is found by finding the shortest distance around the unit circle of pairwise points, as $|\text{diff}(\theta_1, \theta_2)| = |\theta_1 - \theta_2| \leq \pi$. The phase increments are then summed up along a closed path of 4 neighbouring vertices, see Fig. 1. We define counter-clockwise rotations as positive. Algorithmically (indicating translations along axes x, y, z from a point \vec{p} by $\vec{p}_x, \vec{p}_y, \vec{p}_z$ respectively)

⁴We call the phase transition ‘structure-induced’ when $z_{\text{SSB}} \gg z_*$, where z_{SSB} is the actually observed redshift of the phase transition. In a homogeneous universe $z_{\text{SSB}} = z_*$.

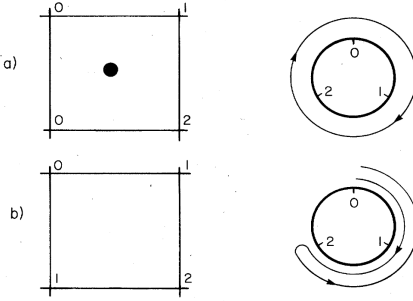


Figure 1: Schematic from [27], indicating the complex phase at four different vertices enclosing a) a string, or b) nothing. Right panel indicates how the path integral goes in either case. When the phase varies continuously there are no phase defects.

```

for  $\vec{p}$  in points
    pathyz = diff( $\vec{p}, \vec{p}_y$ ) + diff( $\vec{p}_y, \vec{p}_{yz}$ ) + diff( $\vec{p}_{yz}, \vec{p}_z$ ) + diff( $\vec{p}_z, \vec{p}$ )
    pathzx = diff( $\vec{p}, \vec{p}_z$ ) + diff( $\vec{p}_z, \vec{p}_{zx}$ ) + diff( $\vec{p}_{zx}, \vec{p}_x$ ) + diff( $\vec{p}_x, \vec{p}$ )
    pathxy = diff( $\vec{p}, \vec{p}_x$ ) + diff( $\vec{p}_x, \vec{p}_{xy}$ ) + diff( $\vec{p}_{xy}, \vec{p}_y$ ) + diff( $\vec{p}_y, \vec{p}$ )
    if pathxy >  $\pi$ 
        stringxy( $\vec{p}$ ) = 1
    else if pathxy <  $-\pi$ 
        stringxy( $\vec{p}$ ) = -1
    ...

```

Using 4 points only, this algorithm is unsuitable for resolving winding numbers $N > 1$. Larger winding numbers are however expected to be rare and short-lived [26], and therefore not important to keep track of here. A similar scheme is applied for finding domain walls in the $\phi \in \mathbb{R}$ simulations, but instead of looking for phase discontinuities, the locations, \vec{p} , where the field χ crosses 0 are identified by the criterion $\text{sign}(\chi(\vec{p}_{-i})\chi(\vec{p}_i)) = \text{sign}(\chi(\vec{p})\chi(\vec{p}_i)) < 0$, where $i \in \{x, y, z\}$ indicates which axis we are comparing along, and $\pm i$ indicates positive or negative increments along this axis. We make sure that it is $\chi(\vec{p})\chi(\vec{p}_i)$ that has different sign among the three in order not to double count the walls at neighbouring points. By comparing three adjacent vertices in the grid, the wall finder algorithm is more robust against spurious detections; in the deeply screened limits or before the phase transition where the field is very small, we expect numerical errors to give some isolated spurious defect detections in both cases of a real and a complex field.

2.3 Parameter choices

As mentioned in Section 1, for the current work, we are interested in the regime of the structure-induced phase transition ($z_{\text{SSB}} \gg z_*$) reported in [23]. In particular, we target the parts of the parameter space where z_{SSB} , being the redshift of the observed phase transition, is $0.5 \lesssim z_{\text{SSB}} \lesssim 0.8$. We can have a rough prediction for z_{SSB} by running smaller box size simulations at the same resolution of $\text{dx} \sim 0.4 h^{-1} \text{Mpc}$. However, the range of underdensities at the smoothing scale of L_C will be increasingly limited by sample variance, which will leave some uncertainty for the actual z_{SSB} in the larger box simulation. This can be alleviated somewhat by running multiple exploratory small box simulations with different seed numbers.

model	z_*	β	L_C [h^{-1} Mpc]	μ [10^{-30} eV]	M [10^{24} eV]	$\lambda \cdot 10^{105}$	$dA_{\phi=v_0} \cdot 10^5$	$V_0 \cdot 10^{12} / \rho_{c,0}$
1_C	0.1	16	1	3.16	6.3	3.7	1.9	2.8
1_R	0.1	16	1	3.16	6.3	3.7	1.9	2.8
2_C	0	50	0.66	4.8	3.6	8.1	6.1	6.7
2_R	0	50	0.66	4.8	3.6	8.1	6.1	6.7
3_R	-0.1	50	0.45	7	2.1	150	2.1	1.7
4_C	-0.1	100	0.45	7	2.1	38	8.2	6.7
5_C	-1/3	1000	0.45	7	1.3	2.3	410	170

Table 1: Choices of parameters for the suite of simulations, using boxsize $B = 500 h^{-1}$ Mpc, and number of grids/particles $N = 1280^3$. The sets of parameters z_* , β , L_C and μ , M , λ can be mapped onto one another one-to-one, and are both stated here for convenience.

The structure-induced, inhomogeneous phase transition, where $z_{SSB} \neq z_*$, occurs when there are significant underdensities at scales $\gg L_C$. In practice, for $L_C \sim 1 h^{-1}$ Mpc, this happens for choices $z_* \lesssim 1$. The smaller z_* , the stronger the screening in overdensities. Being interested in strong screening and environment-dependent effects, we put $z_* \leq 0.1$. This becomes increasingly computationally expensive as smaller z_* means larger effective masses in overdensities, which requires resolving smaller timesteps to capture the phase evolution of the field. Meanwhile, for smaller z_* , one also needs smaller L_C to undergo phase transition at a similar time, which sets a larger mass for the field in underdensities, requiring smaller timesteps to resolve the phase evolution there as well, in addition to requiring better spatial resolution. See [23] for more details. We are limited to $L_C > dx$ and a time step for the scalar field $d\tau \ll dx$ to ensure the stability of the time integration.

The final parameter that we fix is β , which only impacts the vacuum-normalised scalar field's evolution indirectly through the change in the matter configuration; it increases the enhanced clustering of the matter field in the unscreened regions and pushes more matter into the screened regions. As our aim is a proof-of-concept exploration of this lesser known part of the symmetron parameter space, we make sure to pick β large enough to have significant $\sim 4\text{-}15\%$ effects on the matter power spectrum. In practice, it is difficult to establish the exact effect on the matter power spectrum due to the abovementioned sample variance in the smaller tentative box simulations. As we shall see later, simulation 5_C has a very large effect $\Delta P/P \sim 1$, but may still provide phenomenologically interesting observations about the symmetron, relevant to more viable parameter choices.

The final parameter choices are shown in Table 1, where we provide both the choice of phenomenological parameters (z_* , β , L_C) and the equivalent choice of Lagrangian parameters (μ , M , λ) in the units of electronvolts (eV). We also show the difference of the conformal factor from unity, dA , Eq. (2.4), and the size of the symmetron energy barrier, V_0 , Eq. (2.3), setting the overall energy scale of the symmetron sector. The remaining cosmological parameters are chosen according to the Planck Λ CDM best-fit parameters [49], but with number of relativistic species $N_{\text{NCDM}} = 0$ and $N_{\text{eff}} = 3.046$. All simulations parameters will be made available on zenodo after peer-review.

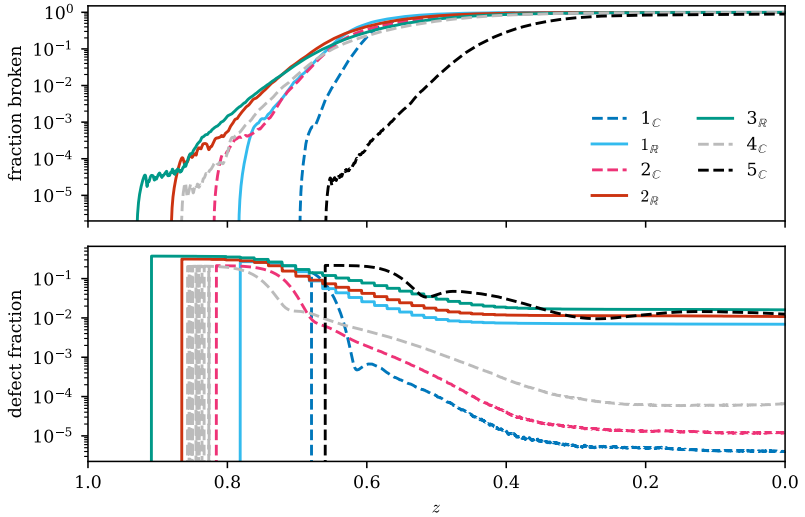


Figure 2: Top: Fraction of the simulation volume where the global $U(1)$ or \mathbb{Z}_2 symmetry is broken, approximated by $|\Re(\chi)| > 10^{-2}$. Bottom: Fraction of simulation volume where phase discontinuities or sign switches are found, respectively in the case of $\phi \in \mathbb{C}$ or $\phi \in \mathbb{R}$.

3 Results

Overview: We show the evolution of the fraction of the simulation volume that has phase transitioned in Fig. 2. The general response to variation of the phenomenological parameters (L_C, z_*, β) is similar to that in the real-valued symmetron case, as shown in [36].

Defect evolution: The evolution of the defect density of the symmetron is shown here for the first time, in Fig. 2. In general, the phase field is smooth before the phase transition, but the defect finder finds a very large defect density in the box as the phase transition occurs⁵. This is followed by a rapid decrease, roughly coinciding with the start of rapid growth of the volume of broken phase (indicated by the field being larger than a threshold value $|\phi| \gtrsim 10^{-2}$). This continues until some lower density plateau, where the defects have taken on a large scale structure as seen in Fig. 3, which occupies more cells in the cases of domain walls. In the very early phase transition, the defect finder finds mostly isolated and disconnected segments of points that fill the volume. They are slowly sorted out by self-annihilation or mergers, leaving in the end only a fraction of more topologically stable extended strings. The process is similar for the case of domain walls. For the strong screening cases of models 3-5, this transition is slowed down, and the defects are still somewhat unformed at redshift $z = 0$, see Fig. 4. This is assisted by the stronger pinning to overdensities that keeps the strings from moving. As time goes on, the defects both move into and become pinned to overdensities, and enhance clustering at their locations. Defects that remain in underdensities without pinning are also unstable and more likely to annihilate. We therefore see in Fig. 5 that the probabilities of the density at the locations of defects start out dominated by underdensities but then move towards larger densities with time. The unnormalised histograms show that

⁵The initial plateau is converged in spatial resolution if assuming that initial defects are 3-dimensional objects, that then evolve into 1-dimensional structures; see appendix B.

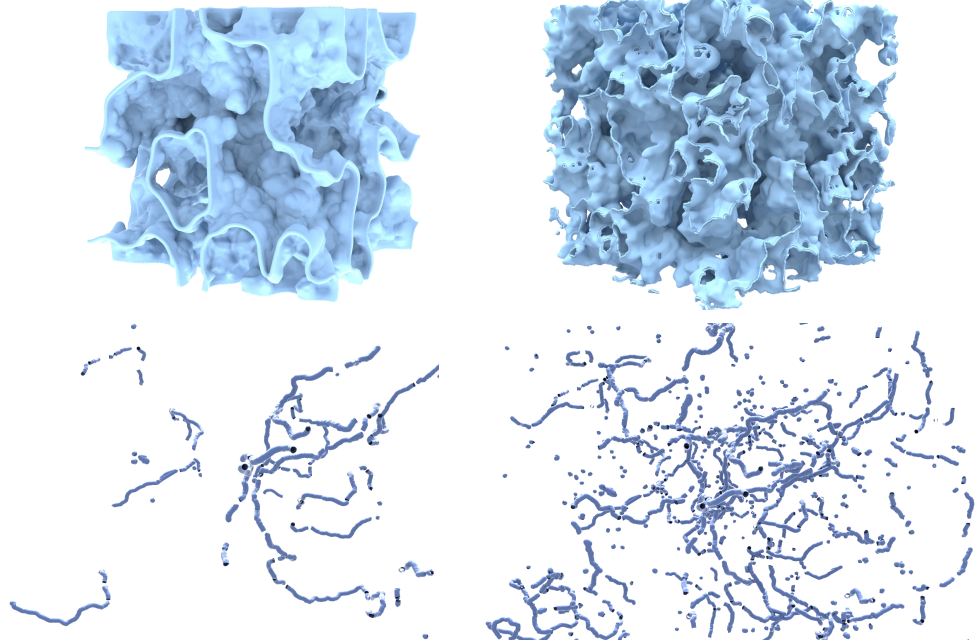


Figure 3: The defect structures that were identified at redshift $z = 0$ for simulations (from top left to bottom right) $1_{\mathbb{R}}$, $2_{\mathbb{R}}$, $1_{\mathbb{C}}$, and $2_{\mathbb{C}}$.

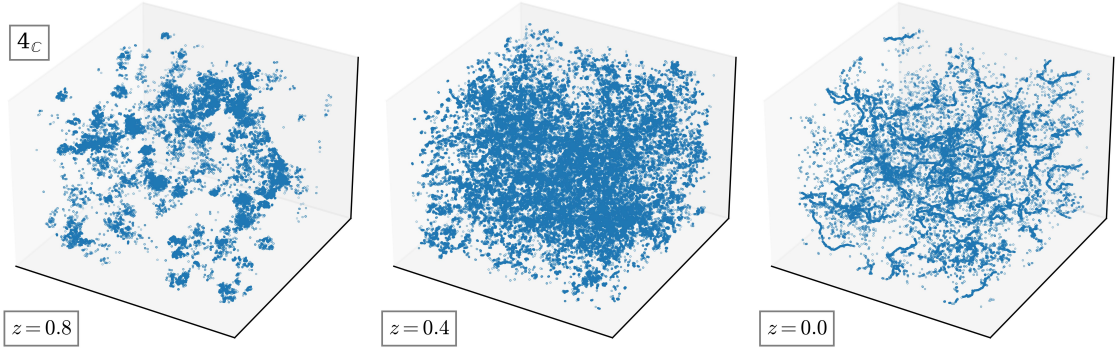


Figure 4: String defects in model $4_{\mathbb{C}}$ at three different redshifts. Strong screening/pinning increases the time for the strings to resolve themselves and assume global structure.

this is both because of a rapid decline of defects at underdensities and a steady growth of number of defects at overdensities, consistent with what Fig. 4 is showing.

Field evolution: The norm of the symmetron field is shown on different timeslices of the simulation volume for models 1 and 2, both $\phi \in \mathbb{R}, \mathbb{C}$, in Fig. 6, while models $3_{\mathbb{R}}-5_{\mathbb{C}}$ are shown in Fig. 7. Comparing $1_{\mathbb{C}}, 2_{\mathbb{C}}$ with $1_{\mathbb{R}}, 2_{\mathbb{R}}$, we notice an almost exact agreement, despite the different field types. At redshift $z = 0.6$, the phase transition has progressed more in the $\phi \in \mathbb{R}$ case for model 1. In Fig. 2, we see that this is always the case $\phi \in \mathbb{R}$ vs. \mathbb{C} , although it is not so clear in Fig. 6, as cases $\phi \in \mathbb{C}$ also have a steeper rise in the fraction of the field

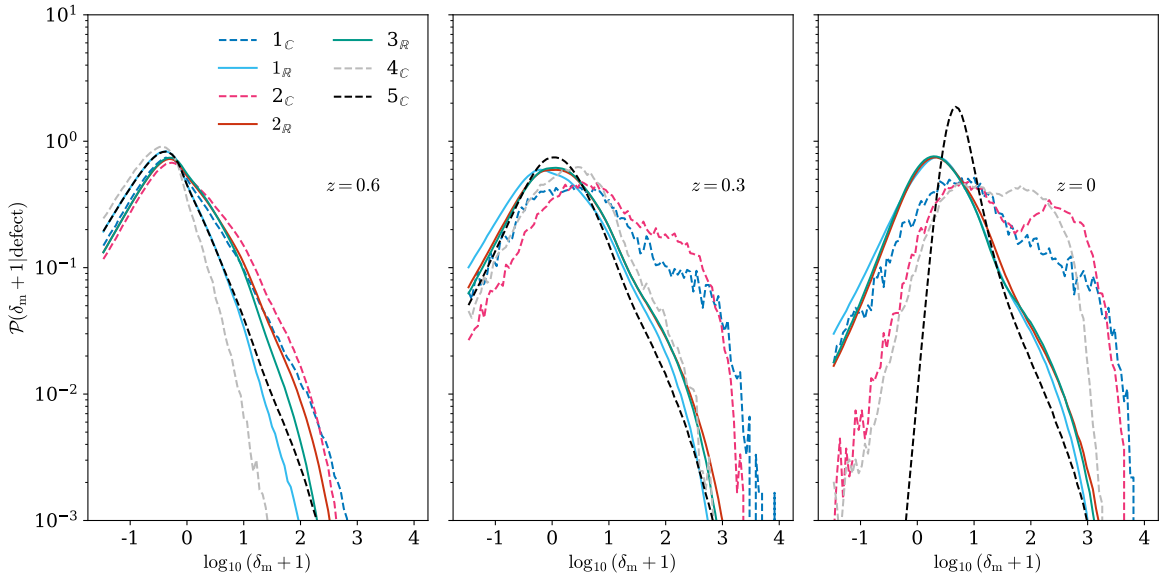


Figure 5: Histograms of the matter overdensity δ_m , at the locations of the identified defects, for different simulations and redshifts.

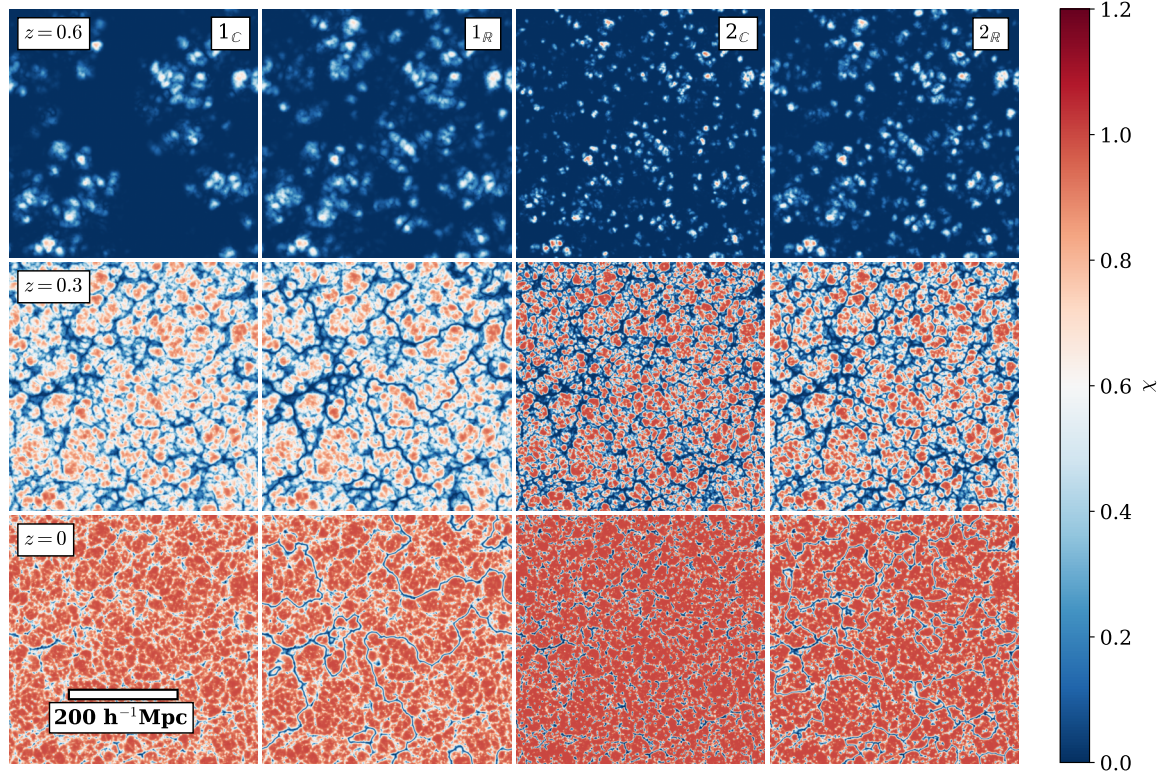


Figure 6: The norm of the scalar field $|\chi|$ for different simulations and redshifts, shown on a slice of the simulation volume.

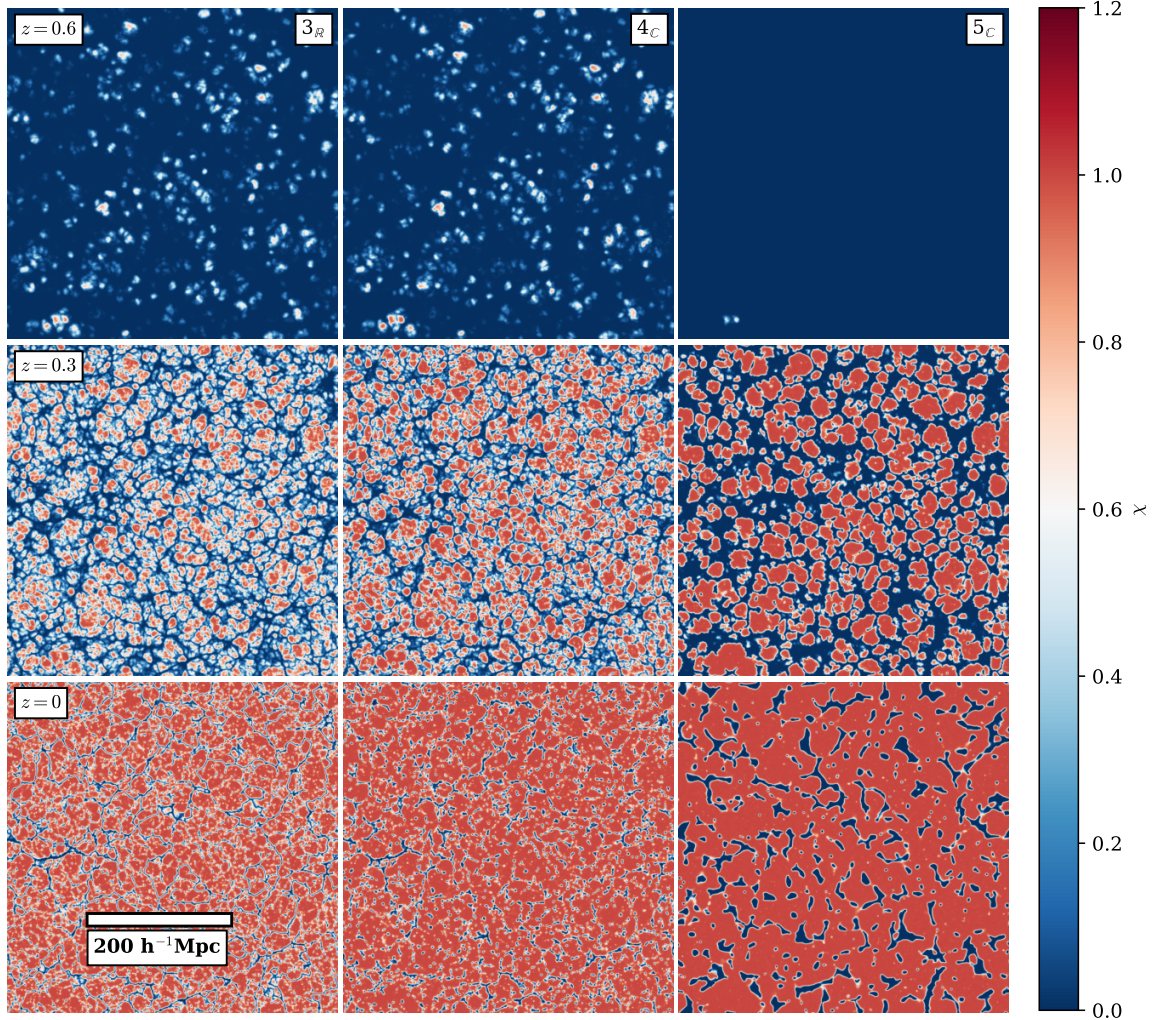


Figure 7: The norm of the scalar field $|\chi|$ for different simulations and redshifts, shown on a slice of the simulation volume.

in the broken phase, and are mostly caught up by redshift $z = 0.6$. At intermediate redshift $z = 0.3$, $\phi \in \mathbb{C}$ vs. \mathbb{R} is almost indistinguishable, at which time mostly isolated domains are growing and barely starting to intersect, encapsulated by overdense regions. However, for both models 1 and 2, it can be seen that the $\phi \in \mathbb{R}$ case has a much more clearly defined cosmic-web-like structure imprinted on it, mostly in places where it is also visible for the $\phi \in \mathbb{C}$ models, indicating the presence of overdensities, and a more effectively screened real-valued scalar field. In some cases the real-valued field has pinned regions where the complex field has none, indicating the presence of domain walls. At redshift $z = 0$, we now see clearly the overdense regions imprinted, with some filaments showing thicker blue arms, likely also representing defects. For the string case, it is more subtle as the defects are 1-dimensional and may extend into the plane.

In Fig. 7, showing models $3_{\mathbb{R}}-5_{\mathbb{C}}$, we no longer compare analogue $\phi \in \mathbb{R}, \mathbb{C}$ simulations. Instead, we are showing a more strongly screened case with a smaller self-interaction range

$L_C = 0.45 h^{-1}$ Mpc. Although the phase transition still occurs⁶ around $z = 0.6$, it is now more progressed in those initial patches, with the encapsulating overdensities to the voids where the initial phase transitions occur, successfully balancing the gradient energy pushing the field to expand, even as the field is fully transitioned $\chi \sim 1$ at $z = 0.6$. This is also the case for $z = 0.3$, where the island domains show $\chi \sim 1$, while in model $1_{\mathbb{C}}$ it was $\chi \sim 0.6$. Finally, at redshift $z = 0$, the domains still successfully expand to cover the entire volume except for overdense filaments and defects. In model $5_{\mathbb{C}}$ that has the strongest screening with $z_* = -1/3$, there are still significant pockets of unbroken volume at $z = 0$. For smaller L_C and z_* still, we expect to prolong the phase transition process further, allowing isolated islands of unscreened domains to persist longer. This can be seen in Fig. 2, when viewing $\phi \in \mathbb{R}, \mathbb{C}$ separately.

3.1 Density distribution

Overview: Figure 8 shows slices of the matter overdensity field at the different redshifts $z = 0.4, 0.2, 0$. For brevity, we show the least extreme cases here, but animations for all simulations are available at the link in footnote 1. At $z = 0.4$, it is difficult to tell a difference between models 1 and Λ CDM, while in model $3_{\mathbb{R}}$, subtle enhanced density contrasts can be seen in the underdensities, coinciding with the initial areas of phase transition of Fig. 7. At redshift $z = 0.2$ the difference from Λ CDM is stark, hollowing out the underdense regions in between filaments significantly by redshift $z = 0$, with overdensities being more concentrated in the cosmic web. The cosmic web itself seems to be less affected and can easily be compared to Λ CDM, though there are some smaller contrasts there. We can see a few filaments that are not visibly present in the Λ CDM case, especially in the $\phi \in \mathbb{R}$ case, likely created by defects. A rich defect network, branching on smaller scales for smaller L_C (as can be seen in Fig. 3) is thus a means of circumventing the hollowing out of underdensities by these strong force strong screening phase transitions. The visibly clear effects in Fig. 8 strongly suggest that the parameter choices made for the simulation suite are constrainable by available datasets. Although our findings below indicate that they are, the signal strength might be weaker than expected from the figure.

Matter structure: We show the relative differences with respect to Λ CDM of the matter power spectra in Fig. 9. The parameter choices were made to have an effect on the matter power spectra $\lesssim 10\%$, which is approximately the case, except for simulation $5_{\mathbb{C}}$ where it was difficult to predict the impact, see the discussion in Section 2.3. Again, simulations 1, 2, $\phi \in \mathbb{C}$ vs. \mathbb{R} are difficult to separate, indicating that the main effect on the matter clustering statistics is not coming from defects, but from the screening profiles of the scalar field as set up by the environment. However, the enhancements found in models 1, 2 for $\phi \in \mathbb{C}$ are 7.3% and 19% larger, respectively, than in their real-valued analogues. This may be due to defects, which in the $\phi \in \mathbb{R}$ case more effectively screens larger volumes, as can be seen by looking at the defect fraction of the box volume in Figs. 2 and 3 or the thicker regions of $\phi \sim 0$ around the filaments in Fig. 6. The enhancement spectra are all initially very peaked at a scale k_* . This scale is seen to vary with L_C between simulations 1, 2 and $3_{\mathbb{R}}$, and scale with the scale factor as a function of the redshift for the individual simulations, since L_C is a physical scale, while k is the comoving wave number. Presumably, this is related to the initial domain size and the region over which ϕ is mostly coherent. We find the scale to be well approximated by $k_* \simeq (5L_C)^{-1}(a_*/0.909)^{-2}$; it is not clear whether the scaling will persist for a wider range of

⁶Figure 2 shows several models that have 10^{-5} - 10^{-3} of the volume in the broken phase since $z \sim 0.8$ - 0.9 .

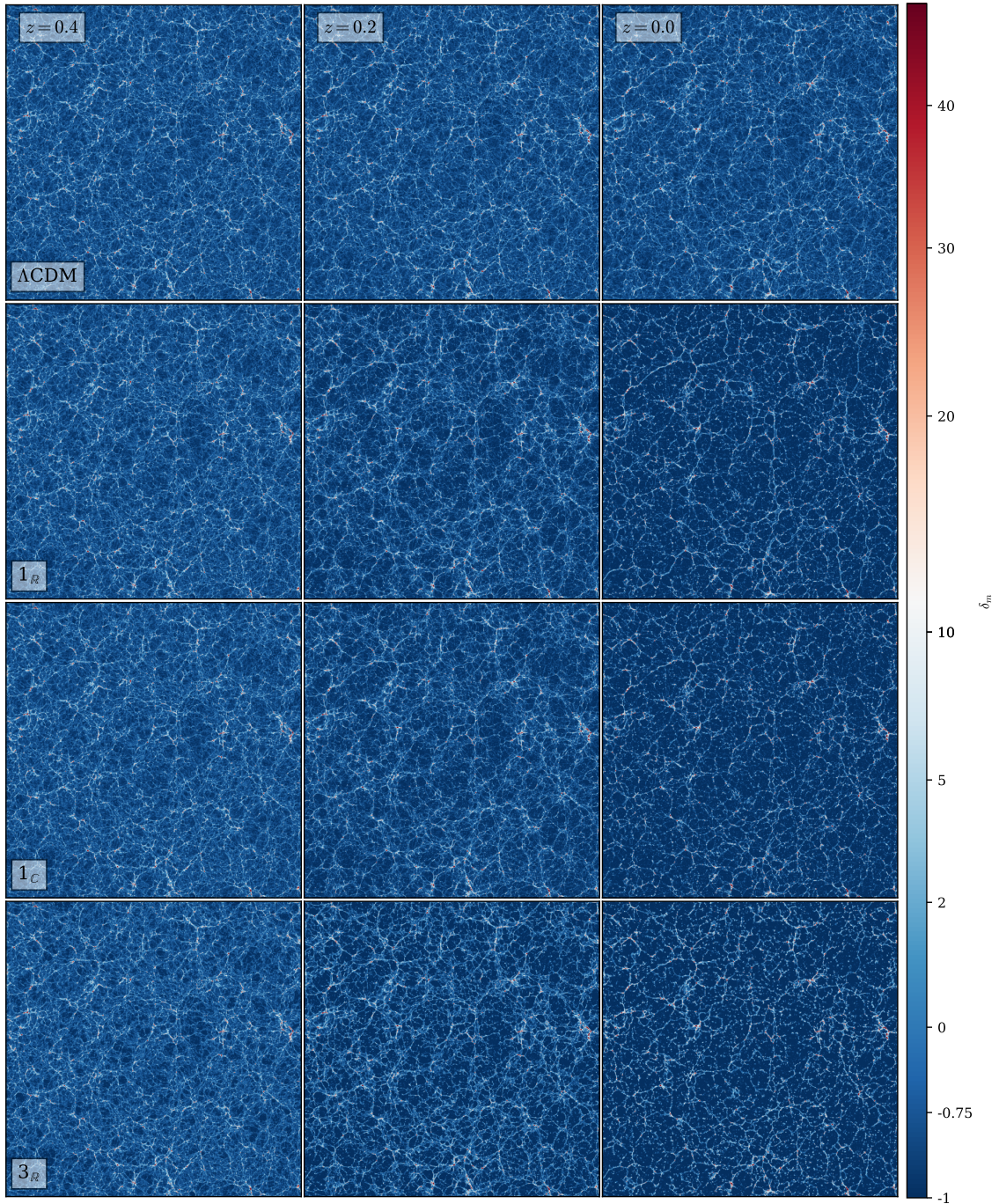


Figure 8: The matter overdensity δ_m for 3 redshifts $z = 0.4, 0.2, 0$ for a selection of the simulation suite.

parameters. The high- k growth of power in Fig. 9 is a resolution effect as we approach the Nyquist frequency at $8 h \text{ Mpc}^{-1}$. The drop in power before this relates to efficient screening at small scales and in the case of simulation 5_C in particular because of the destruction of small-scale structures from the strong forces and matter flows.

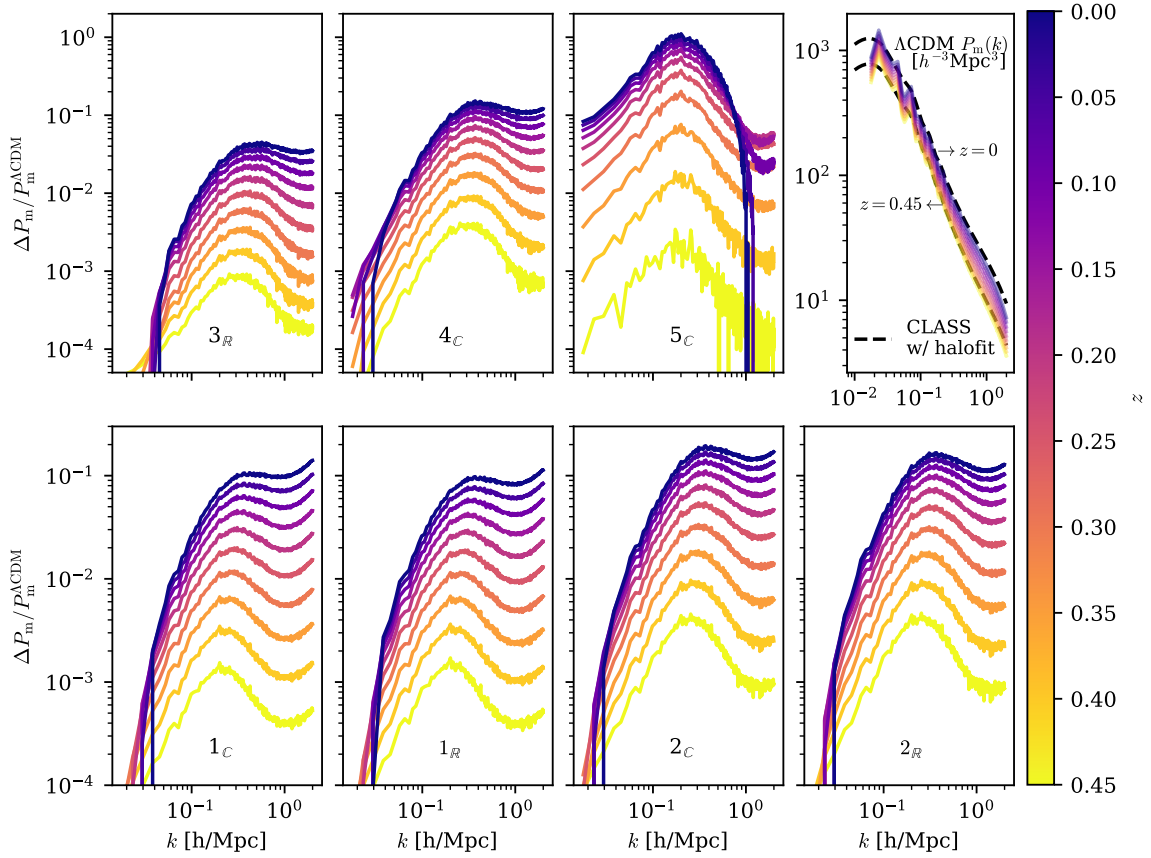


Figure 9: Relative differences in matter power spectra, shown for the different simulations in panels 1-4. The colour indicates the redshift, from 0.45 to 0. The Nyquist frequency is $k_{\text{Nyq}} \approx 8 h \text{ Mpc}^{-1}$. All of the spectra show enhancement with respect to the ΛCDM case. Top right panel: The ΛCDM power spectra $P_m(k)$ for the same redshift range, compared to CLASS with halofit at $z = 0.45$ and $z = 0$.

Matter velocities: In Fig. 10 we show modified velocity statistics of matter particles as a consequence of being accelerated by the fifth force. Error bars are generated from the variances found in delete-one jackknife sampling, on sub-volumes created by splitting the simulation box into 16 equal rectangular rods. The bars show 95% error intervals. We see a clear growth of a large velocity tail, larger mean, and log-normal appearance for all simulations. Simulation 5_C in particular forms a second peak at larger velocities that has a larger area than the original peak by redshift $z = 0$.

Nonlinear structures: Figure 8 described in the first paragraph of Section 3.1 shows large relative effects on the matter distribution in the underdense environments for the non- ΛCDM choices, while the overdense filaments are mostly intact. Here we investigate the effect on virialised structures or matter halos, which predominantly form in overdense environments. The `Rockstar` halo finder [50] identifies halos in simulation snapshots by constructing phase-space trees of gravitationally bound particles. The gravitational binding used in `rockstar` is found assuming ΛCDM using the standard `rockstar` halo definition, which comes with some caveats and should be modified in a more complete approach. After compiling the

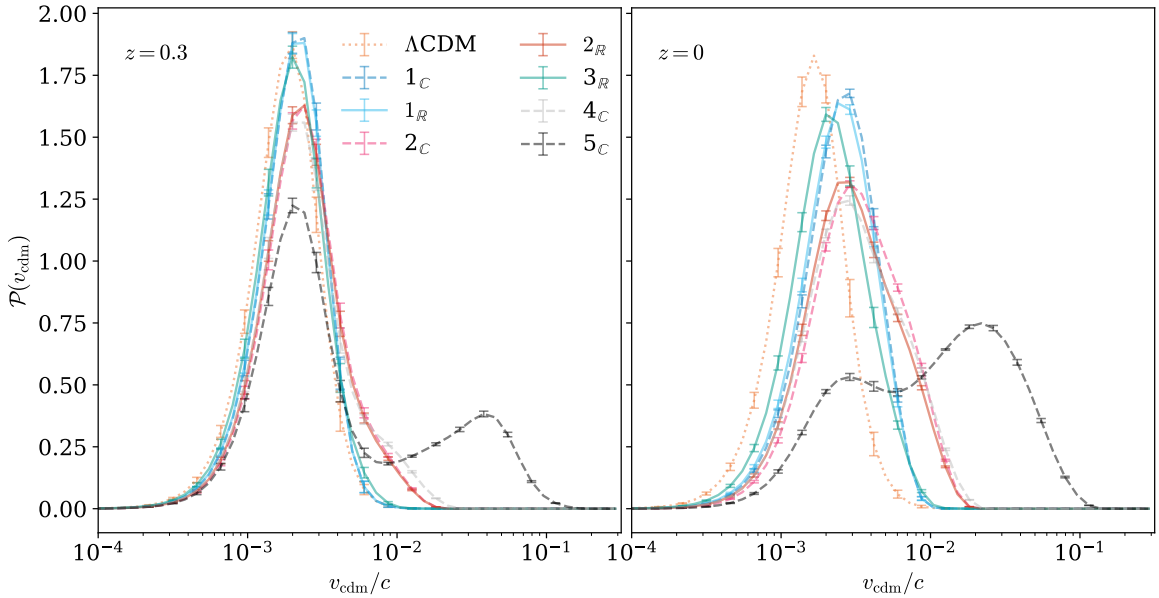


Figure 10: Velocity histograms of the cold dark matter particles at different redshifts, normalised to probability distributions. Error bars show 2σ intervals in the jackknife scatter. Logarithmic scale is chosen to highlight the appearance of a second peak in model 5_C .

full halo catalogues, we remove subhalos bound to parent halos from our analysis. We use the mass definition m_{200b} that defines the mass of the halo as the mass enclosed within the largest spherical shell within which the average matter density is 200 times greater than the background density. The halo finder finds halos with more than 50 particles while putting the force resolution to $dx_F = 0.06 h^{-1}\text{Mpc}$, which is smaller than the one suggested by the grid spacing by a factor of 4 in order to have sufficiently large catalogues, with the caveat that some of the smaller halos can be a result of noise. For now, we are looking at summary statistics and not substructure, which allows less conservative resolution settings. We select the $N = 500\,000$ most massive halos from each halo catalogue for the analysis, except for the halo mass functions, where we keep all halos. In comparing different simulations, fixing the number of halos is the more observationally relevant comparison, and is the closer analogue to a survey where they would observe a number of galaxies limited by their luminosities.

Halo mass function: Figure 11 shows the Halo Mass Functions (HMFs) of the halo catalogues at redshifts $z = 0.3$ and $z = 0$. The mass function is shown and compared to the parametrisation of Tinker et al. [51] in the case of ΛCDM , while each of the other simulations is given in terms of relative difference with respect to the simulation of ΛCDM . There is a clearly defined peak in the HMF enhancement, where the abundance of halos is significantly enhanced with respect to ΛCDM , in most scenarios. This peak appears to shift towards larger masses with time. Counter-intuitively, halo masses smaller than the peak appear to be suppressed rather than enhanced, but we only observe this effect in the simulations where $\phi \in \mathbb{C}$. Indeed, in all cases, there are smaller enhancements for $\phi \in \mathbb{C}$ than for $\phi \in \mathbb{R}$. This is clear when comparing simulation variants of simulations 1, 2 that differ only in this respect. Simulations 3_R and 4_C also show this trend, even as simulation 4_C has twice as large a fifth force strength parameter β . The effect on the HMF of simulation 4_C remains within $\sim 10\%$

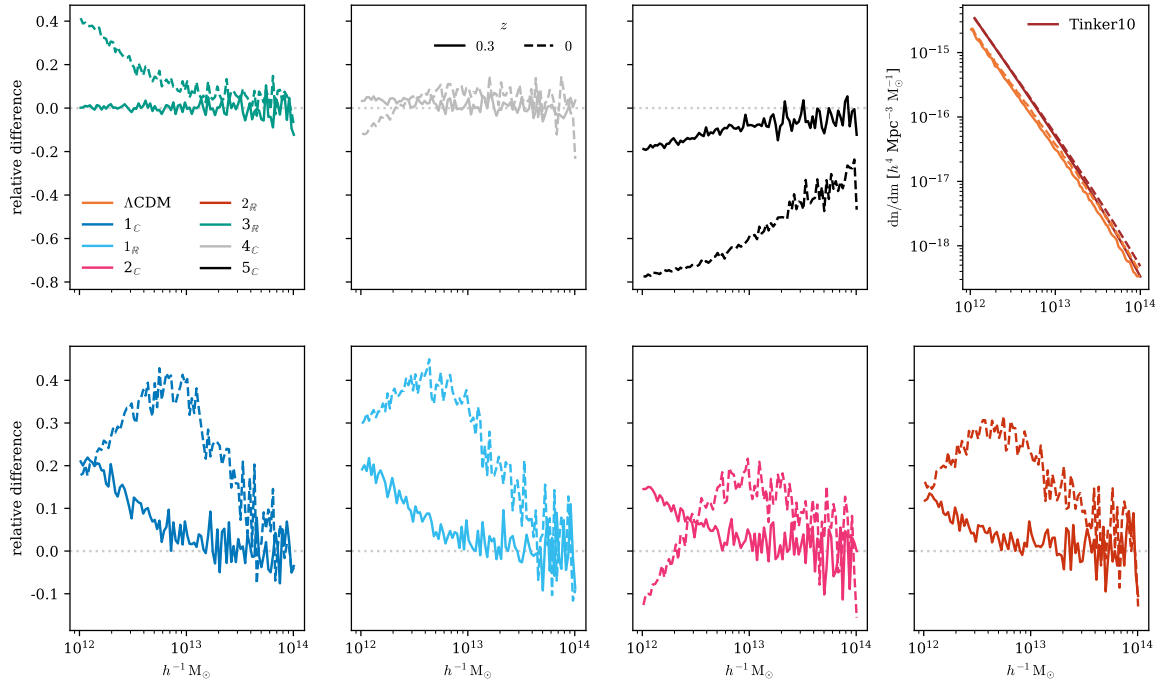


Figure 11: Top: Halo mass functions dn/dm for different simulations (colour) and redshifts (linestyle), as a function of the solar mass M_\odot . Bottom: Relative differences with respect to the Λ CDM case. Halos with masses $M \ll 10^{13} h^{-1} M_\odot$ are poorly resolved and should be interpreted carefully.

of Λ CDM, despite the more dramatic effects on the matter density distribution than seen in Fig. 8. Simulation 5_C is again the most extreme case and shows a suppression across all masses.

Understanding the reason for the suppression in the HMF for model 5_C and for low masses for models $2_C, 4_C$ requires running more careful analysis of the many contributing effects to their formation and migration away from underdense areas. One should also explore the effect of modifying the `Rockstar` halo binding energy, which in the presence of the fifth force may allow larger velocity particles to bind to a halo. These are interesting future directions that are outside of the scope of the current work. The above observations should furthermore be taken with the caveat that the small mass halos (less than $\sim 10^{13} h^{-1} M_\odot$) are poorly resolved, see e.g. the growing mismatch with the Tinker mass function at smaller masses, Fig. 11. Optimistically, the relative differences are less sensitive to resolution effects, but ideally these trends should be investigated in simulations with larger dynamical ranges of scales and a more conservative halo definition.

Halo velocities: Figure 12 shows the velocity distributions of the halo catalogues at the different redshifts $z = 0.3, 0$, with error bars produced in the same way as for the matter velocity distribution, Fig. 10. At $z = 0.3$, the effect on their velocity dispersion is very marginal and consistent with each other within $1-2\sigma$ error bars, apart from simulation 5_C that is barely 2σ lower in amplitude at the peak of the distribution. At redshift $z = 0$, only simulation 3_R has a compatible distribution with Λ CDM, while the rest follow more tailed distributions, with velocities reaching percent of the speed of light. For comparison,

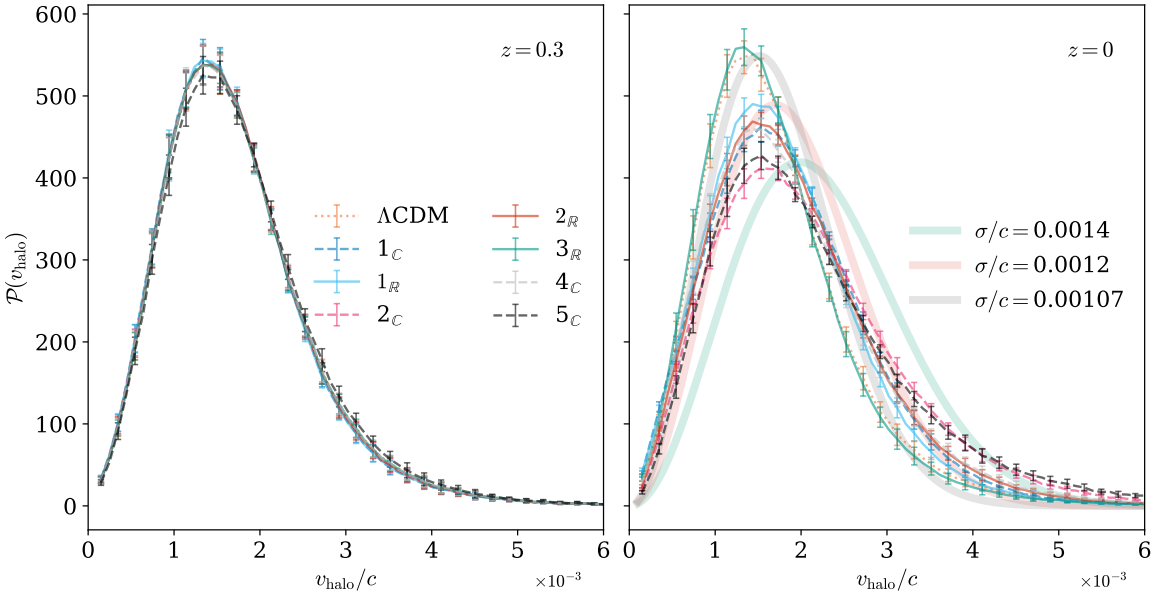


Figure 12: Velocity histograms of 500 000 most massive halos at redshifts $z = 0.3, 0$, normalised to probability distributions. Shown here for the different simulations. Error bars show 2σ intervals in the jackknife scatter.

Maxwell-Boltzmann distributions with different velocity dispersion σ_v/c are overlaid in wide bands, showing that the different simulations range from $\sim 12\text{--}30\%$ larger effective velocity dispersion in the halo catalogues, compared to ΛCDM . This will likely cause observable effects in galaxy surveys, where galaxy velocities cause redshift space distortions in the reconstructed halo positions, and the appearance of a characteristic quadrupole in the effective distribution [52].

3.2 Probes of environment-dependent effects

In the previous section, we presented $\sim 10\text{--}20\%$ effects on summary statistics such as matter power spectra and velocity histograms (excluding simulation 5_C for now). The abundance of halos is more affected, with effects of up to $\sim 40\%$. However, the halo abundances in simulations 2 and 4_C are affected only at 20% and 10%, respectively. Figure 8 shows more dramatic but very environment-dependent effects on the density distribution. In this section, we will investigate whether environment-dependent probes can capture this signal successfully and thus become target probes for constraining SIPT-type models qualitatively similar to the ones presented here.

Matter density PDF: A Gaussian probability distribution is uniquely defined in terms of its mean and variance. The typical scenario in study is that of adiabatically sourced, Gaussian initial density perturbations produced by cosmological inflation, and subsequently acted upon by linear physics. Power spectra and 2-point correlation functions are therefore widely used in cosmological analysis. In the late-time Universe nonlinearities grow and cause the density distribution to acquire non-Gaussian features [53]. Recent and upcoming surveys, e.g. Euclid [54], are therefore increasingly targeting nonlinear statistics such as bispectra or voids distributions. The nonlinearities may also be accessed by considering the Probability

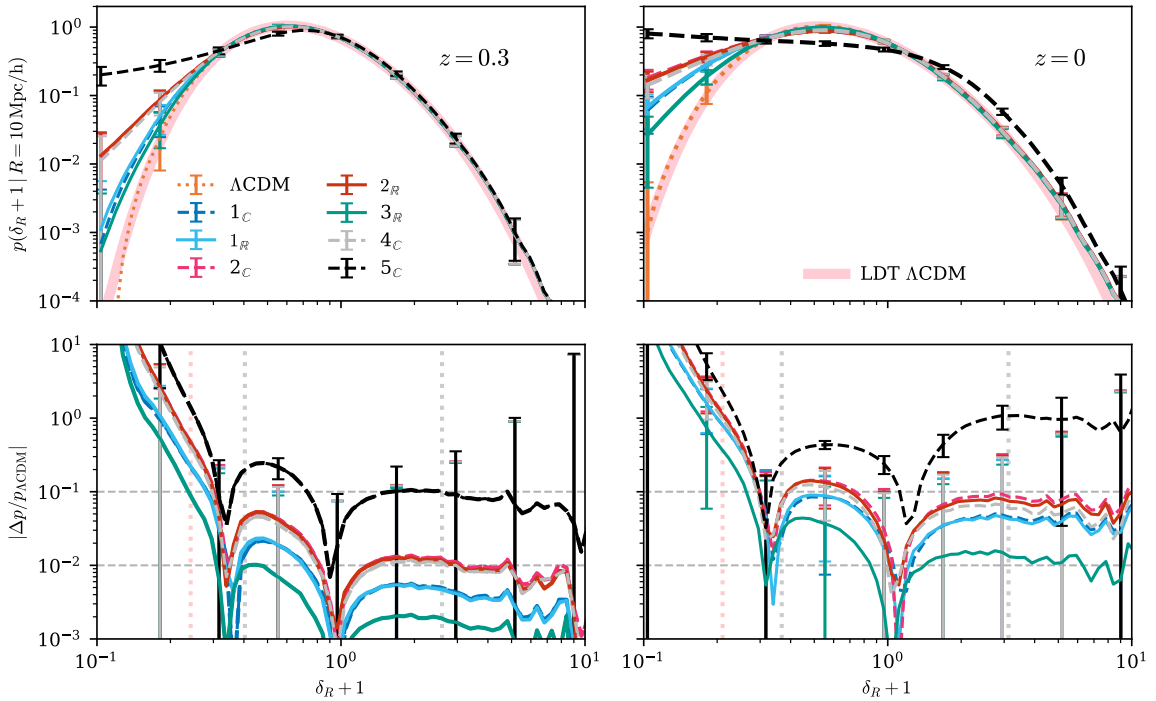


Figure 13: Density histograms of the density fields of matter for the different models and redshifts. The density fields are smoothed with a spherical top-hat filter of $R = 10 h^{-1} \text{ Mpc}$ radius. Top row: The density probabilities. Bottom row: The relative differences of the density probabilities with respect to the ΛCDM model case. The dotted vertical lines indicate the 1%, 3% and 90% quantiles of the respective ΛCDM CDFs $c(\delta_R > x; z)$. Errorbars indicate 2σ intervals in the Poisson noise.

Density Function (PDF) – or equivalently the 1-point distribution function. Analytic predictions for the PDF can be made using Large Deviations Theory (LDT) [55, 56]. This gives us a window into environment-dependent physics by encoding nonlinear physics such as the density-dependent screening of the symmetron. We follow the procedure laid out in [57]: first, we smooth the overdensity field from our simulations with a top-hat smoothing window; then, we generate the PDF of the resulting overdensity field. For comparison, we apply the Python package `pyLDT-cosmo` by [57], to which we have to input log-density variances found in our simulation snapshots.

In Fig. 13, we show the 1-point distribution function, or the PDF, for a density field that is smoothed with a top-hat filter with smoothing radius $R = 10 h^{-1} \text{ Mpc}$. The predictions for ΛCDM are made using the variance of the log-density distribution $S_2 \equiv \text{Var}(\log[1 + \delta_m])$. At redshifts $z = 0$ and $z = 0.3$, the ΛCDM simulation gives $S_2^{z=0} = 0.379226$ and $S_2^{z=0.3} = 0.291989$, respectively. Compared with the variance reported for $z = 0$ in table B1 of [57], ours is 3.3% smaller, which we assume is due to our different simulation setup and slightly different cosmological parameters. We find good agreement with the LDT prediction for the ΛCDM simulation. The small differences may be due to our particle-mesh-based code, compared to the `Quijote` simulation suite used in [57] which uses the tree-PM force solver of `Gadget-3`, in turn based on `Gadget-2` [58]. Additionally, low probabilities $p \ll 10\%$ are increasingly subject to sample variances from the finite simulation volume. We indicate the

sample variance of the limited number, N , of independent spheres of the smoothing radius inside of the box volume per bin $\Delta\delta_R$, with the formula $\sigma_{\text{PDF}} = \sqrt{n_i/(N_{\text{sphere}} \Delta\delta_R)}$, where n_i is the bin count of the i th simulation. We approximate N_{sphere} by the volume fraction $N_{\text{sphere}} \approx V_{\text{box}}/V_{\text{sphere}}$. Relative differences to ΛCDM ($i = 0$) are estimated using the formula $\sigma_{\text{rel}} = \sqrt{n_i/n_0^2 + n_i^2/n_0^3}$, which can be derived from Eq. (8) in [59] after inserting $\mu_i = n_i$ and $\sigma_i = \sqrt{n_i}$ for the mean and standard deviation. Compared to our ΛCDM simulation, the PDFs of the different models 1-2 and 3-5 all have a large enhancement in underdensities $\delta_R \lesssim -0.65$, reaching 100% for $z = 0$ at $\delta_R \sim -0.75, -0.9$ depending on the model, and reaching a factor ~ 10 by $\delta_R \lesssim -0.85$. A pattern of enhancement can be seen at small and large densities, and suppression at intermediate densities $-0.7 \lesssim \delta_R \lesssim 0$. We note that the signal is too small to beat sample variance for the relative differences at $z = 0.3$ (apart from simulation 5_C), but it becomes significant for $\delta_R \lesssim -0.3$ at $z = 0$.

PDF detectability: In Section 5.6 of [60] a short discussion of applicability to survey data is provided. An option is to find the weak-lensing convergence PDF in tomographic redshift slices, as was done in [61]. As discussed there, this is in particular relevant to the Euclid survey [54] that will provide accurate weak-lensing measurements over half the age of the Universe. This is less relevant for our case as the Euclid survey will cover redshifts $z = 0.9$ -1.8. Instead, e.g. SDSS data (total redshift range $z = 0$ -0.7) can be applied; this was done with count-in-cell PDFs of galaxies in [62]. Finally, ‘density-split statistics’ combines the two approaches to relate the galaxy count PDF to the matter density PDF. The Fisher analysis in [60] was made directly on the matter PDFs, discarding the 3% smallest densities and 10% largest densities, as they found them to be the most sensitive to resolution effects. The 3 and 90 percentiles of the Cumulative Distribution Functions (CDFs) are indicated in the lower panels of Fig. 13, showing that the main signal of our models would thus be discarded in this analysis. For the percentiles that would be included, the signal of our models is ~ 0.1 -1% and 1-10% at redshifts $z = 0.3, 0$, respectively, which is greater than the effects of $\sim 2\%$ for the massive neutrino models shown in Fig. 10 of [60]. By combining three redshifts, three smoothing radii, and the matter power spectra up to quasilinear scales, they claim a BOSS-like survey ($z = 0.15$ -0.7) can put a 5σ lower constraint on the sum of neutrino masses, which is impacting the matter PDF at ~ 1 -2%. Although these late-time phase transition (SIPT) models are active for a shorter time duration and thus benefit less from the boosted signal and the removal of degeneracies by the use of multiple redshifts, it is still likely that they are distinguishable from ΛCDM by using their large signal at very small redshifts. Extending the analysis to include lower percentile density data will significantly boost the signal, but this is more subject to sample variance as the tails of the PDF correspond to rarer events. The DESI Bright Galaxy Survey (BGS) catalogue covers the redshift range $0.1 < z < 0.3$. A lower bound on the sample variance can be made by counting the number, N_{sphere} , of $R = 10 h^{-1}$ Mpc spheres in the corresponding comoving survey volume (which is greater than our simulation box). Ignoring masking and sky coverage, we find $N_{\text{sphere}} \sim 5.6 \times 10^5$, corresponding to a Poisson relative error of $\Delta p/p \sim \pm 10\%$ at 2σ for a 1% quantile (smallest quartile is shown by red vertical line in Fig. 13). This comes on top of the uncertainties related to tracer sampling and systematics that can be significant. However, the signal is $\mathcal{O}(1)$, which is likely to be sufficiently large for detection. While interesting, a full Fisher analysis forecast of detectability of these structure induced symmetron models is beyond the scope of this paper.

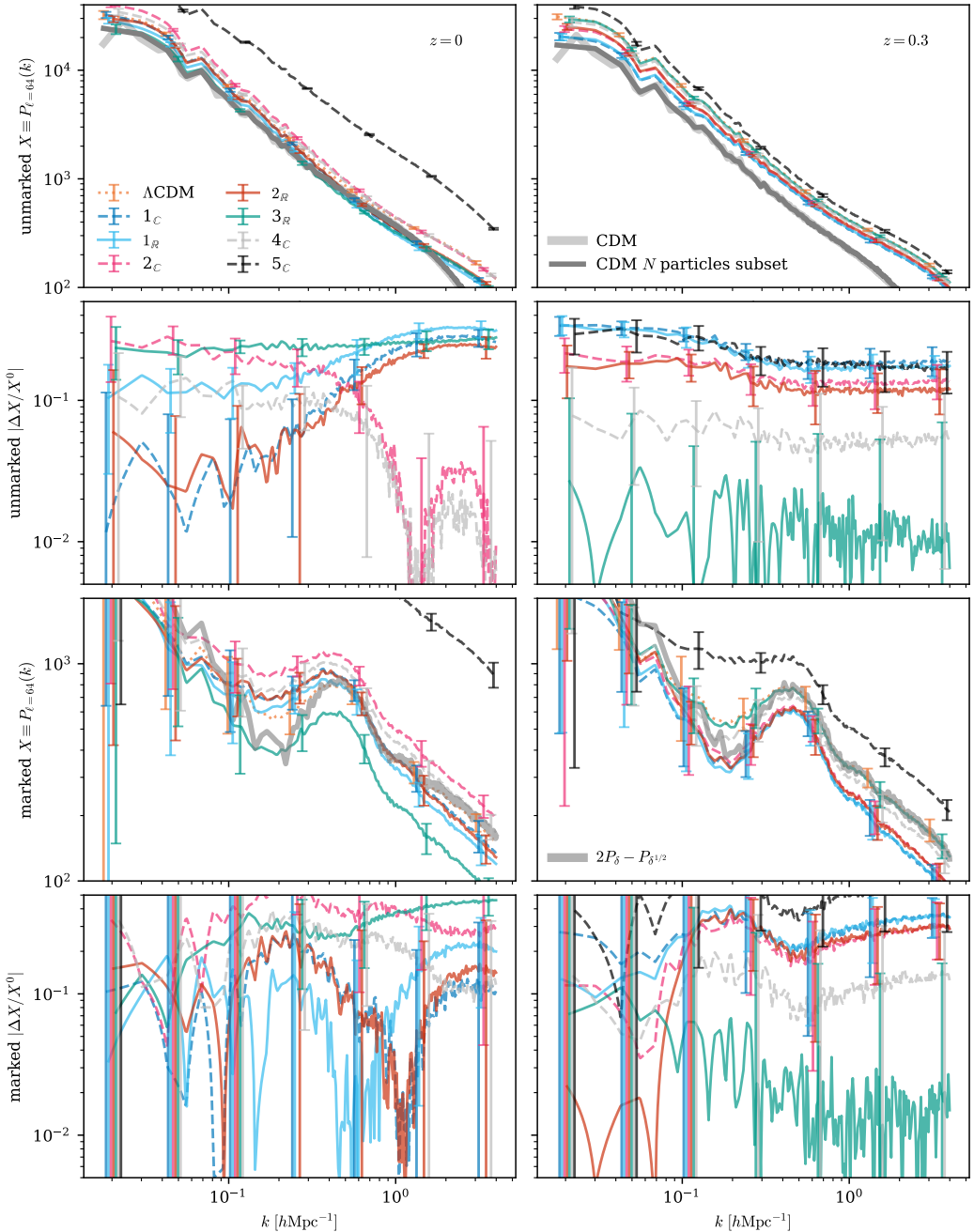


Figure 14: Halo power spectra for the different models at redshifts $z = 0$ and $z = 0.3$. Errorbars represent 2σ jackknife scatter. Top row: Monopole power spectra of the halo catalogues in the different models. The thick solid grey lines show the spectra computed from *all* particles and from a random subset of 500 000 particles, respectively. Second row: Absolute relative differences of the power spectra between the models at the two redshifts, with respect to the Λ CDM case. Bottom rows: Same as top rows, but for the marked halo power spectra, using the mark defined in Eq. (3.1).

Halo spectra and marked statistics: A second approach to boosting the signal strength for environment-dependent physics is using marked power spectra [63]. In this approach we are finding the summary statistics of a field that is transformed (marked) as $\delta_m \rightarrow m(\delta_m, \dots) \delta_m$. In [64] a specific mark was suggested for probing environment-dependent screening models of modified gravity

$$m(x; R, p, \delta_s) = \left(1 + \frac{\delta_R(x)}{1 + \delta_s}\right)^{-p}, \quad (3.1)$$

where δ_R again is the density field smoothed with a top-hat filter over a radius R , δ_s parametrises the sensitivity of the mark to the local density and larger exponents $|p|$ give more environmentally sensitive weights. Positive p are up-weighting underdense environments, which is beneficial in our case as this is where the most dramatic effects occur; see Fig. 8. In [65] 125 different choices of the parameters R, δ_s, p were considered for the case of massive neutrinos, and the choice $R = 10 h^{-1} \text{Mpc}$, $p = 2$ and $\delta_s = 0.25$ was found to give the tightest constraints on cosmological parameters. An exhaustive study of optimal weight choices is beyond the scope of our work. Instead, as a proof of concept, we will adopt the mark (3.1) with parameters $R = 10 h^{-1} \text{Mpc}$, $p = 2$, $\delta_s = 0.25$.

Both marked and unmarked halo density power spectra are shown in Fig. 14. They are found, as described in the start of this subsection, from the $N_h = 500\,000$ most massive halos in the simulation. For each unmarked power spectrum, there is expected a shot noise contribution due to the limited tracer number $P_{\text{SN}} = V/N_h$, where V is the simulation volume. We are here removing this by splitting the halo population into two random subsamples that we cross-correlate. Their respective shot-noise contributions will be uncorrelated and thus disappear in the cross-correlation. This agrees with the result we get by subtracting the shot noise from the full population auto-correlation. As an additional check, we find good agreement between the full set of matter particles' power spectrum and the spectrum found by randomly selecting $N = N_h$ matter particles and performing the cross-correlation procedure on this sample. In the marked case, the marks change the noise properties of the spectra. Assuming independence of the weights and tracers one can find the analytic generalisation of the shot noise contribution $P_{\text{SN}} = V\langle m^2 \rangle / (\langle m \rangle^2 N_h)$ [66]. In reality, the marks and tracers are highly correlated by design, which can introduce scale-dependent shot-noise and require a more careful modelling. We again do the split-population cross-correlation in the marked case to remove any linear contributions from the shot noise. The remaining noise is estimated from the variance found in 16 delete-1 jackknife samples. As an indication of residual shot noise level, we plot for ΛCDM the spectrum $2P_\delta - P_{\delta^{1/2}}$, where P_δ is the auto-spectrum of the full population and $P_{\delta^{1/2}}$ that of half of the population. This should subtract the shot noise contribution in the case where it is predominantly a linear addition, and it agrees with the cross-correlation result within the jackknife-estimated error. There is a particular good agreement on large k , but deviations of size of the overall signals on smaller $k \lesssim 5 \times 10^{-1}$. Indeed, the jackknife errors indicate that the signal to noise vanishes in this range. As such, these scales may be better explored in larger halo catalogs $N_h \gg 5 \times 10^5$, or with better nonlinear noise treatment.

The ΛCDM halo catalogue has a linear bias $b_0 \approx 1.07$ compared to the matter density field, when matched in the unmarked spectra on scales $k < 0.4 h \text{Mpc}^{-1}$ at $z = 0$. The population at $z = 0.3$ has a linear bias $b_{0.3} \approx 1.27$. In general, we see a greater sensitivity to the SIPT-type symmetron in the halo spectra relative to ΛCDM than in the matter power spectra, Fig. 9. The unmarked halo spectra, Fig. 14, show both relative enhancements and suppressions. Model $3_{\mathbb{R}}$, which has the weakest signal in the matter power spectrum, has one

of the strongest overall signals in the halo spectrum at $z = 0$, showing a nearly scale-invariant suppression at 20-25%, while being sub-percent at redshift $z = 0.3$. Other models, such as 1, 2, are expressed most strongly on large scales at $z = 0.3$, while peaking on small scales at $z = 0$. Model 4_C stands out as a model that is less strongly expressed in the halos than the matter particles, staying below 10% here, while having matter power spectra enhanced at $\sim 15\%$. All models, apart from 5_C, show initial suppression of halo clustering at redshift $z = 0.3$, while 2_C and 4_C have enhanced halo clustering by $z = 0$. The marked spectra are mostly successfully boosting the signal at scales close to $k \sim \pi/(2R) \sim 0.15 h \text{ Mpc}^{-1}$, while sometimes weakening the signal at smaller and larger scales. The improved signal strength at large scales in the marked case at $z = 0.3$, is a factor $\sim 5\text{-}10$ for model 3_R, while more modest for the rest. At redshift $z = 0$, model 1_C and model 2_R are improving by a factor ~ 10 at large scales, while e.g. models 3_R and 1_R seem overall worse. Unfortunately, most of the gain of the marked cases is lost in the larger jackknife errors, with the unmarked spectra performing better overall when error is included. This is likely to improve on the use of larger tracer catalogues.

Halo spectra detectability: Matter halos are not directly accessible in observations, but are hosting clusters of galaxies that are. Connecting the effects on the halo statistics to those of accessible tracers like galaxies requires an abundance matching scheme, see, e.g. [67]. For simplification, here we did a mass-ranked abundance matching, where we assume that the N largest mass dark matter halos are hosting the N brightest central galaxies that would be detected in a magnitude-limited galaxy survey, dismissing e.g. satellite galaxies. Galaxy survey catalogues are composed of galaxies at different redshifts according to radial distance, which has the potential to dilute the overall signal for wide redshift bins and models that go from halo clustering power suppression to enhancement, such as 2_C and 4_C. Smaller redshifts, where we are seeing stronger effects, are limited by small observational survey volumes. Although the Euclid survey is expected to have sub-percent errors on the galaxy spectrum measurements at scales smaller than $k \sim 0.45 h \text{ Mpc}^{-1}$, it will only take data between $z = 0.9\text{-}1.8$ [54], within which our current selection of models mimics ΛCDM , apart from possible foreground effects. The BOSS galaxy survey, see, e.g. [68], covers smaller redshifts $z = 0.15\text{-}0.7$, and the DESI survey has galaxy catalogues starting at $z \sim 0.1$. In [16], the DESI full-shape analysis was performed in 6 redshift bins, where the magnitude-limited BGS has $0.1 < z < 0.4$, and the lowest redshift bin of Luminous Red Galaxies (LRG) has $0.4 < z < 0.6$. The rest of the bins have $z > 0.6$ and would thus be insensitive to this selection of models. Taking into account the reduced data in the lower redshift, it is still likely that the DESI and SDSS data can detect deviations from ΛCDM : At large scales ($k \lesssim 0.1 h \text{ Mpc}^{-1}$), the DESI BGS has a similar number of tracers to us ($N_t \sim 3 \times 10^5$) and an effective redshift $z_{\text{eff}} \sim 0.3$. Figure 17 of [69] shows that the statistical and systematic 2σ errors are roughly $\pm 5\%$ at $k \sim 0.1 h \text{ Mpc}^{-1}$, which can be further reduced by using larger k -bins. While large (1-30 %), several of the relative signals shown in Fig. 14 are approximately constant on these scales; in this case, the effect can be absorbed into a redefinition of the halo bias b . Breaking this degeneracy requires additional measurements, for example through Redshift-Space Distortions (RSD). A more comprehensive analysis accounting for this is interesting but beyond the scope of the present work. The marked spectra seem promising because they give moderate to large enhancements of the signal, but the larger jackknife errors indicate that the effect of shot noise is amplified, requiring either larger tracer catalogues, or a better treatment of the nonlinear shot noise.

4 Summary and conclusion

The case of an inhomogeneous and structure-induced phase transition (SIPT), where $z_{\text{SSB}} \gg z_*$, presents us with an interesting model case to confront with observational data, where environment-dependent effects are in the front seat. Although the symmetron model was studied in particular here, our results should be kept in mind when developing other late-time phase transition models (with e.g. non-perturbative potentials or conformal factors). Our main findings can be summarised as follows.

Model

- SIPT-type models may be applied to address the coincidence problem of dark energy by coupling the phase transition to nonlinear structure formation. But achieving energy densities relevant for dark energy requires non-perturbative conformal factors and/or potentials, as discussed in Sections 1-2.
- The SIPT-type symmetron can generate very structured and small-scale defect networks that pin to overdensities and do not enter the scaling regime. They can therefore maintain a high defect density with cosmic time. Their late formation and relatively low energy scale avoids issues with overclosing of the Universe.
- The defect densities in SIPT-type models depend on the densities of initially isolated voids that are sufficiently underdense at the time of its phase transition. This is set by both the phase transition energy ρ_* (or z_*) and the Compton wavelength L_C , see e.g. Figs. 2-3. The defect density is insensitive to the causal horizon and is therefore different from the usual phase transition models that make use of the Kibble mechanism.
- $\phi \in \mathbb{R}$ tends to have better screening properties than $\phi \in \mathbb{C}$, due to the larger volume coverage of the wall defects compared to the string defects, and steeper field profiles when approaching overdensities (see Fig. 15 for defect profiles).
- Large defect densities can be achieved and applied to enter a regime where topological screening is more important, presumably to a much greater extent than what was explored here.

Phenomenology

- We have observed a migration of defects to locations with greater ambient densities over time (see Fig. 5).
- The strong coupling/strong screening regime tends to have large effects on the velocity dispersion of cold dark matter particles (Fig. 10) and smaller but still large effects on the halo velocity dispersion (Fig. 12) as the halos tend to form in the higher density, screened regions.
- The halo formation is mostly enhanced due to the fifth force enhancing clustering and increasing the matter infall into overdense regions. However, in some cases, we are seeing the formation of halos suppressed, presumably due to the strong acceleration of particles in underdense regions, which is more pronounced for $\phi \in \mathbb{C}$ that has less steep screening and defect profiles, see e.g. Fig. 15. However, this interpretation requires a more careful analysis to verify, see the discussion in Section 3.1.
- Underdense regions where the phase transition is occurring are dramatically more empty than they would be in Λ CDM (Fig. 8), which is visible in the low-density tail of the PDF, Fig. 13.

- Different models can affect different probes very differently. For example model $3_{\mathbb{R}}$ where the global dark matter power spectrum is only changed with respect to Λ CDM at a $\sim 4\%$ level (Fig. 9), the halo mass function shows 40% effects for small masses. We see 20-25% effects on the halo spectra at $z = 0$, while it is sub-percent at $z = 0.3$.
- A flat enhancement of the halo power spectrum can be absorbed into the linear halo bias parameter, requiring additional probes, such as RSD, to disentangle the degeneracy.

Environment-dependent probes

- As discussed in Subsection 3.2, effects that appear exclusively at low redshift are observationally more challenging due to the smaller survey volumes. This shows up as large sample variance in both of our environment-dependent probes.
- Assuming that the effects we found generalise to the cases of galaxy spectra and the PDF estimators, it is likely that the full set of models considered here can be constrained by currently available data.
- Less extreme choices of the matter coupling β will be consistent with the observed galaxy power spectra and other standard probes while giving strong effects in underdense regions, motivating the continued development of environment-dependent probes such as one-point PDFs, marked statistics and analyses based on voids.
- SIPT-type models like the symmetron make an interesting test case for the development of such probes, and may be used as a proxy for other models inducing strong environment-dependent effects in the late-time Universe.

In conclusion, we have shown that SIPT-type dark sector phase transitions can couple modifications of Λ CDM cosmology to nonlinear structure formation, generating dense and persistent string or wall defect networks that evade standard Kibble scaling. The phase transition induces strong environment-dependent effects, which we investigate using the matter PDF and marked halo statistics. These models can leave only modest imprints on traditional large-scale observables while producing dramatic modifications in underdense regions, halo properties, and velocity statistics at late times. As a result, the inclusion of environment-dependent probes is expected to allow strong constraints on even more subtle parameter choices (such as smaller coupling β). In particular the detection of the low-density tail of the PDFs emerges as a key observational target. Observables such as matter density PDFs, marked statistics, and void-based analyses are therefore essential. SIPT-type models provide a compelling and well-controlled framework for developing and testing such probes, with broader relevance for any late-time physics that couples the dark sector to underdense environments.

Acknowledgements: *\emptyset .C. thanks Hans Winther for useful discussions. This work was co-funded by the European Union and supported by the Czech Ministry of Education, Youth and Sports (Project No. FORTE – CZ.02.01.01/00/22_008/0004632). J.A. acknowledges funding by the Swiss National Science Foundation and the Dr. Tomalla Foundation for Gravity Research. M.K. acknowledges funding by the Swiss National Science Foundation. This work was supported by a grant from the Swiss National Supercomputing Centre (CSCS) under project ID sm97 on Alps, and by the Ministry of Education, Youth and Sports of the Czech Republic through the e-INFRA CZ (PiD:FTA-25-52).*

References

- [1] Y.B. Zeldovich, *The Cosmological constant and the theory of elementary particles*, *Sov. Phys. Usp.* **11** (1968) 381.
- [2] S. Weinberg, *The Cosmological Constant Problem*, *Rev. Mod. Phys.* **61** (1989) 1.
- [3] S.P. Martin, *A Supersymmetry primer*, *Adv. Ser. Direct. High Energy Phys.* **18** (1998) 1 [[hep-ph/9709356](#)].
- [4] B.A. Bassett, M. Kunz, J. Silk and C. Ungarelli, *A Late time transition in the cosmic dark energy?*, *Mon. Not. Roy. Astron. Soc.* **336** (2002) 1217 [[astro-ph/0203383](#)].
- [5] L. Perivolaropoulos and F. Skara, *Gravitational transitions via the explicitly broken symmetron screening mechanism*, *Phys. Rev. D* **106** (2022) 043528 [[2203.10374](#)].
- [6] G. Alestas, I. Antoniou and L. Perivolaropoulos, *Hints for a Gravitational Transition in Tully–Fisher Data*, *Universe* **7** (2021) 366 [[2104.14481](#)].
- [7] C. Burrage, E.J. Copeland and P. Millington, *Radial acceleration relation from symmetron fifth forces*, *Phys. Rev. D* **95** (2017) 064050 [[1610.07529](#)].
- [8] C. Burrage, E.J. Copeland, C. Käding and P. Millington, *Symmetron scalar fields: Modified gravity, dark matter, or both?*, *Phys. Rev. D* **99** (2019) 043539 [[1811.12301](#)].
- [9] C. Käding, *Lensing with Generalized Symmetrons*, *Astronomy* **2** (2023) 128 [[2304.05875](#)].
- [10] K. Hinterbichler and J. Khoury, *Symmetron Fields: Screening Long-Range Forces Through Local Symmetry Restoration*, *Phys. Rev. Lett.* **104** (2010) 231301 [[1001.4525](#)].
- [11] K. Hinterbichler, J. Khoury, A. Levy and A. Matas, *Symmetron Cosmology*, *Phys. Rev. D* **84** (2011) 103521 [[1107.2112](#)].
- [12] D. Tong, *String Theory*, [0908.0333](#).
- [13] B. Bertotti, L. Iess and P. Tortora, *A test of general relativity using radio links with the Cassini spacecraft*, *Nature* **425** (2003) 374.
- [14] G. Esposito-Farese, *Tests of scalar-tensor gravity*, *AIP Conf. Proc.* **736** (2004) 35 [[gr-qc/0409081](#)].
- [15] S. Tsujikawa, K. Uddin, S. Mizuno, R. Tavakol and J. Yokoyama, *Constraints on scalar-tensor models of dark energy from observational and local gravity tests*, *Phys. Rev. D* **77** (2008) 103009 [[0803.1106](#)].
- [16] DESI collaboration, *DESI 2024 VII: cosmological constraints from the full-shape modeling of clustering measurements*, *JCAP* **07** (2025) 028 [[2411.12022](#)].
- [17] DESI collaboration, *DESI 2024: reconstructing dark energy using crossing statistics with DESI DR1 BAO data*, *JCAP* **10** (2024) 048 [[2405.04216](#)].
- [18] M. Ishak et al., *Modified gravity constraints from the full shape modeling of clustering measurements from DESI 2024*, *JCAP* **09** (2025) 053 [[2411.12026](#)].
- [19] A. Chudaykin and M. Kunz, *Modified gravity interpretation of the evolving dark energy in light of DESI data*, *Phys. Rev. D* **110** (2024) 123524 [[2407.02558](#)].
- [20] G. Ye, M. Martinelli, B. Hu and A. Silvestri, *Hints of Nonminimally Coupled Gravity in DESI 2024 Baryon Acoustic Oscillation Measurements*, *Phys. Rev. Lett.* **134** (2025) 181002 [[2407.15832](#)].
- [21] W.J. Wolf, C. García-García, T. Anton and P.G. Ferreira, *Assessing Cosmological Evidence for Nonminimal Coupling*, *Phys. Rev. Lett.* **135** (2025) 081001 [[2504.07679](#)].
- [22] Ø. Christiansen, F. Hassani and D.F. Mota, *Environmental cosmic acceleration from a phase transition in the dark sector*, *JCAP* **01** (2025) 043 [[2405.00668](#)].

[23] Ø. Christiansen, F. Hassani and D.F. Mota, *Asimulation: Domain formation and impact on observables in resolved cosmological simulations of the (a)symmetron*, *Astron. Astrophys.* **689** (2024) A6 [[2401.02410](#)].

[24] J. Adamek, C. Clarkson, L. Coates, R. Durrer and M. Kunz, *Bias and scatter in the Hubble diagram from cosmological large-scale structure*, *Phys. Rev. D* **100** (2019) 021301 [[1812.04336](#)].

[25] A. Vilenkin, *Cosmic Strings and Domain Walls*, *Phys. Rept.* **121** (1985) 263.

[26] M.B. Hindmarsh and T.W.B. Kibble, *Cosmic strings*, *Rept. Prog. Phys.* **58** (1995) 477 [[hep-ph/9411342](#)].

[27] T. Vachaspati and A. Vilenkin, *Formation and Evolution of Cosmic Strings*, *Phys. Rev. D* **30** (1984) 2036.

[28] R. Durrer, M. Kunz and A. Melchiorri, *Cosmic structure formation with topological defects*, *Phys. Rept.* **364** (2002) 1 [[astro-ph/0110348](#)].

[29] T. Vachaspati, *Kinks and Domain Walls : An Introduction to Classical and Quantum Solitons*, Oxford University Press (2007), [10.1017/9781009290456](#).

[30] A. Nezhadsafavi and L. Pogosian, *Cosmic strings in the complex symmetron model*, *Phys. Rev. D* **112** (2025) 043528 [[2504.19830](#)].

[31] C. Llinares and L. Pogosian, *Domain walls coupled to matter: the symmetron example*, *Phys. Rev. D* **90** (2014) 124041 [[1410.2857](#)].

[32] C. Llinares and D. Mota, *Releasing scalar fields: cosmological simulations of scalar-tensor theories for gravity beyond the static approximation*, *Phys. Rev. Lett.* **110** (2013) 161101 [[1302.1774](#)].

[33] C. Llinares, D.F. Mota and H.A. Winther, *ISIS: a new N-body cosmological code with scalar fields based on RAMSES. Code presentation and application to the shapes of clusters*, *Astron. Astrophys.* **562** (2014) A78 [[1307.6748](#)].

[34] C. Llinares and D.F. Mota, *Cosmological simulations of screened modified gravity out of the static approximation: effects on matter distribution*, *Phys. Rev. D* **89** (2014) 084023 [[1312.6016](#)].

[35] R. Teyssier, *Cosmological hydrodynamics with adaptive mesh refinement: a new high resolution code called RAMSES*, *Astron. Astrophys.* **385** (2002) 337 [[astro-ph/0111367](#)].

[36] Ø. Christiansen, F. Hassani, M. Jalilvand and D.F. Mota, *Asevolution: a relativistic N-body implementation of the (a)symmetron*, *JCAP* **05** (2023) 009 [[2302.07857](#)].

[37] J. Adamek, D. Daverio, R. Durrer and M. Kunz, *General relativity and cosmic structure formation*, *Nature Phys.* **12** (2016) 346 [[1509.01699](#)].

[38] J. Adamek, D. Daverio, R. Durrer and M. Kunz, *gevolution: a cosmological N-body code based on General Relativity*, *JCAP* **07** (2016) 053 [[1604.06065](#)].

[39] J. Adamek, R. Durrer and M. Kunz, *N-body methods for relativistic cosmology*, *Class. Quant. Grav.* **31** (2014) 234006 [[1408.3352](#)].

[40] D. Daverio, M. Hindmarsh and N. Bevis, *Latfield2: A c++ library for classical lattice field theory*, [1508.05610](#).

[41] Ø. Christiansen, J. Adamek, F. Hassani and D. Mota, *Gravitational waves from dark domain walls*, *JCAP* **01** (2025) 149 [[2401.02409](#)].

[42] C. Llinares and P. Brax, *Detecting Coupled Domain Walls in Laboratory Experiments*, *Phys. Rev. Lett.* **122** (2019) 091102 [[1807.06870](#)].

[43] C. Burrage, B. March and A.P. Naik, *Accurate computation of the screening of scalar fifth forces in galaxies*, *JCAP* **04** (2024) 004 [[2310.19955](#)].

[44] F. Hassani, J. Adamek, M. Kunz and F. Vernizzi, *k-evolution: a relativistic N-body code for clustering dark energy*, *JCAP* **12** (2019) 011 [[1910.01104](#)].

[45] A. Nouri-Zonoz, F. Hassani, E. Bellini and M. Kunz, *KGB-evolution: a relativistic N-body code for kinetic gravity braiding models*, [2511.04676](#).

[46] L. Reverberi and D. Daverio, *fRevolution – Relativistic Cosmological Simulations in f(R) Gravity I: Methodology*, *JCAP* **07** (2019) 035 [[1905.07345](#)].

[47] Ø. Christiansen, *Cosmological Simulations of Phase Transitions in Screened Scalar-Tensor Gravity: Cosmic acceleration, topological defects, gravitational waves and relativistic observables*, doctoral thesis, University of Oslo, 2024.

[48] K. Choi, S.H. Im and C. Sub Shin, *Recent Progress in the Physics of Axions and Axion-Like Particles*, *Ann. Rev. Nucl. Part. Sci.* **71** (2021) 225 [[2012.05029](#)].

[49] PLANCK collaboration, *Planck 2018 results. VI. Cosmological parameters*, *Astron. Astrophys.* **641** (2020) A6 [[1807.06209](#)].

[50] P.S. Behroozi, R.H. Wechsler and H.-Y. Wu, *The Rockstar Phase-Space Temporal Halo Finder and the Velocity Offsets of Cluster Cores*, *The Astrophysical Journal* **762** (2013) 109.

[51] J.L. Tinker, A.V. Kravtsov, A. Klypin, K. Abazajian, M.S. Warren, G. Yepes et al., *Toward a halo mass function for precision cosmology: The Limits of universality*, *Astrophys. J.* **688** (2008) 709 [[0803.2706](#)].

[52] N. Kaiser, *Clustering in real space and in redshift space*, *Mon. Not. Roy. Astron. Soc.* **227** (1987) 1.

[53] F. Bernardeau, *The Gravity induced quasi-Gaussian correlation hierarchy*, *Astrophys. J.* **392** (1992) 1.

[54] EUCLID collaboration, *Euclid. I. Overview of the Euclid mission*, *Astron. Astrophys.* **697** (2025) A1 [[2405.13491](#)].

[55] F. Bernardeau and P. Reimberg, *Large deviation principle at play in large scale structure cosmology*, *Phys. Rev. D* **94** (2016) 063520 [[1511.08641](#)].

[56] C. Uhlemann, S. Codis, C. Pichon, F. Bernardeau and P. Reimberg, *Back in the saddle: Large-deviation statistics of the cosmic log-density field*, *Mon. Not. Roy. Astron. Soc.* **460** (2016) 1529 [[1512.05793](#)].

[57] M. Cataneo, C. Uhlemann, C. Arnold, A. Gough, B. Li and C. Heymans, *The matter density PDF for modified gravity and dark energy with Large Deviations Theory*, *Mon. Not. Roy. Astron. Soc.* **513** (2022) 1623 [[2109.02636](#)].

[58] V. Springel, *The Cosmological simulation code GADGET-2*, *Mon. Not. Roy. Astron. Soc.* **364** (2005) 1105 [[astro-ph/0505010](#)].

[59] E. Díaz-Francés and F.J. Rubio, *On the existence of a normal approximation to the distribution of the ratio of two independent normal random variables*, *Statistical Papers* **54** (2013) 309.

[60] C. Uhlemann, O. Friedrich, F. Villaescusa-Navarro, A. Banerjee and S. Codis, *Fisher for complements: Extracting cosmology and neutrino mass from the counts-in-cells PDF*, *Mon. Not. Roy. Astron. Soc.* **495** (2020) 4006 [[1911.11158](#)].

[61] A. Barthelemy, S. Codis, C. Uhlemann, F. Bernardeau and R. Gavazzi, *A nulling strategy for modelling lensing convergence in cones with large deviation theory*, *Mon. Not. Roy. Astron. Soc.* **492** (2020) 3420 [[1909.02615](#)].

[62] A. Yang and W.C. Saslaw, *The galaxy counts-in-cells distribution from the SDSS*, *Astrophys. J.* **729** (2011) 123 [[1009.0013](#)].

[63] D. Stoyan, *On Correlations of Marked Point Processes*, *Mathematische Nachrichten* **116** (1984) 197.

[64] M. White, *A marked correlation function for constraining modified gravity models*, *JCAP* **11** (2016) 057 [[1609.08632](#)].

[65] E. Massara, F. Villaescusa-Navarro, S. Ho, N. Dalal and D.N. Spergel, *Using the Marked Power Spectrum to Detect the Signature of Neutrinos in Large-Scale Structure*, *Phys. Rev. Lett.* **126** (2021) 011301 [[2001.11024](#)].

[66] O.H.E. Philcox, E. Massara and D.N. Spergel, *What does the marked power spectrum measure? Insights from perturbation theory*, *Phys. Rev. D* **102** (2020) 043516 [[2006.10055](#)].

[67] R. Stiskalek, H. Desmond, T. Holvey and M.G. Jones, *The dependence of subhalo abundance matching on galaxy photometry and selection criteria*, *Mon. Not. Roy. Astron. Soc.* **506** (2021) 3205 [[2101.02765](#)].

[68] O.H.E. Philcox and M.M. Ivanov, *BOSS DR12 full-shape cosmology: Λ CDM constraints from the large-scale galaxy power spectrum and bispectrum monopole*, *Phys. Rev. D* **105** (2022) 043517 [[2112.04515](#)].

[69] DESI collaboration, *DESI 2024 V: Full-Shape galaxy clustering from galaxies and quasars*, *JCAP* **09** (2025) 008 [[2411.12021](#)].

[70] R. Durrer, *Topological defects in cosmology*, *New Astronomy Reviews* **43** (1999) 111.

[71] H.B. Nielsen and P. Olesen, *Vortex Line Models for Dual Strings*, *Nucl. Phys. B* **61** (1973) 45.

A String profile

In order to validate the implementation of the model in the code, we start by solving a simple string on a homogeneous background. By assuming an axisymmetrical system, following [70], also covered in [26, 30], one can semi-analytically solve the scalar profile of a string. One finds the quasistatic equation of motion, where the Laplacian is put in polar (and comoving) coordinates

$$\partial_r^2 \phi + \frac{1}{r} \partial_r \phi + \frac{1}{r^2} \partial_\theta^2 \phi = a^2 V_\phi. \quad (\text{A.1})$$

If we make the Nielsen-Olesen ansatz [71] that the only azimuthal dependence is for the phase, which does not have radial dependence, then $\phi = v f(r) e^{in\varphi}$, where φ is the phase, n is the winding number, $v \equiv \frac{\mu}{\sqrt{\lambda}}$ is the vacuum expectation value, while f is the radial field profile. Defining the radial coordinate $s = rv$ gives the equation for the profile

$$f_{,ss} + \frac{1}{s} f_{,s} - \frac{n^2}{v^2} f - a^2 \lambda f (f^2 - [1 - \bar{\rho}_m/\rho_*]) = 0. \quad (\text{A.2})$$

We can solve this as an initial boundary value problem with $f(r = \infty), f_{,s}(r = \infty) = v, 0$ and $f(r = 0), f_{,s}(r = 0) = 0, 0$. We put the winding number $n = 1$. For the symmetron parameters $(L_C, z_*, \beta) = (1 h^{-1}\text{Mpc}, 2, 8)$, we find the profile shown in the left panel of Fig. 15. For the simulation, we initialise the scalar field in four quadrants at $z = 0.4$ at its background minimum $|\phi| = v_0 \sqrt{1 - \rho_m(z)/\rho_*}$. We use a homogeneous density field $\rho_m(z) = \Omega_m \rho_{c,0}/a^3$. The four quadrants are initialised at different phase angles $\varphi = \pi/2, \pi, 0, -\pi/2$, from upper right quadrant and clockwise. Then Gauss-Seidel relaxation (see [36]) is iterated until a tolerance $|\chi_{i+1} - \chi|_{\max} < 10^{-8}$ is reached. This is done in a boxsize of $B = 300 h^{-1}\text{Mpc}$, and a spatial resolution $dx = 1.5 h^{-1}\text{Mpc}$. This is less than our spatial resolution criterion $dx/L_C < 1$ that we keep in our dynamical simulations. Figure 15 shows string defects forming after relaxation at a regular grid at the intersections of the four quadrants (with periodic boundary conditions). The string profile is seen to match well with the analytical expectation (left panel).

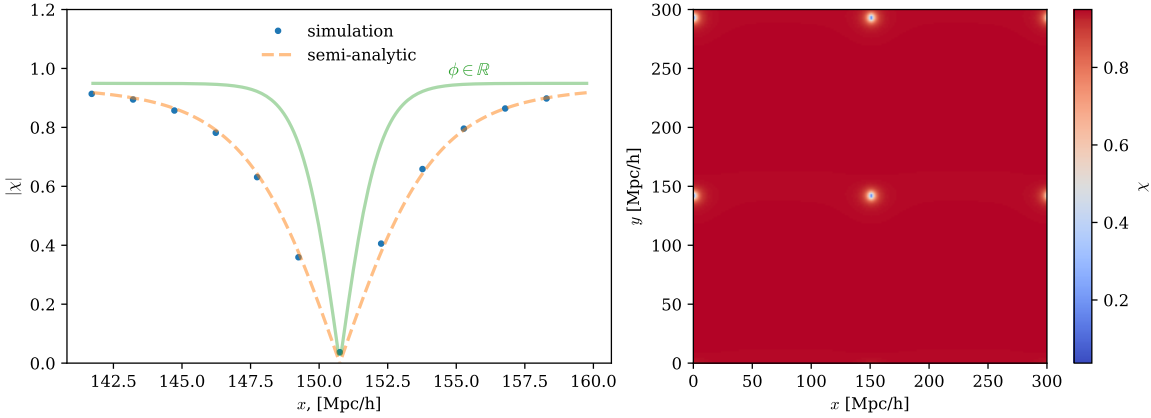


Figure 15: Quasistatic field $|\chi| = |\phi|/v_0$ after relaxing it using Gauss-Seidel relaxation. Left panel: field profile of centre-most string defect, orthogonal to the defect axis. We compare with the semi-analytic profile found from the ODE derived in [70]. Green line shows the analytic profile of the real-valued field $\phi \in \mathbb{R}$. Right panel: grid of strings formed after the relaxation.

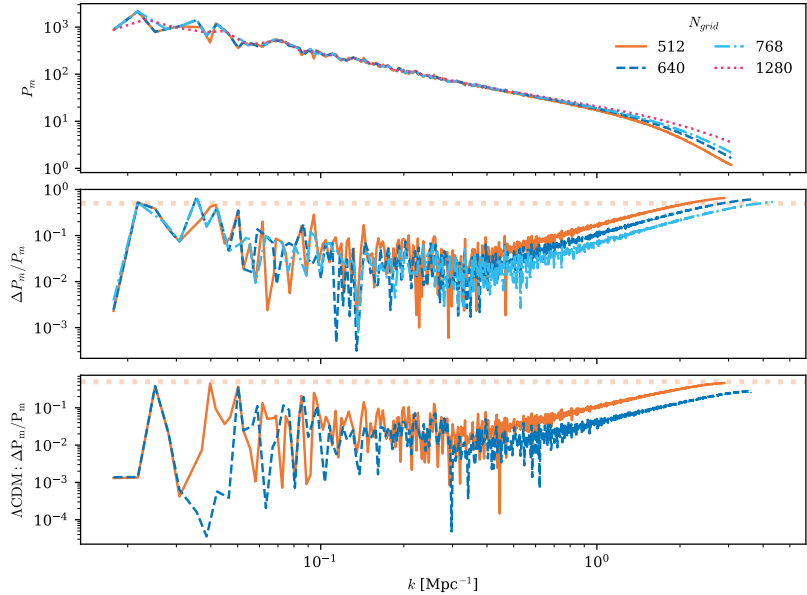


Figure 16: Convergence of matter power spectrum with increasing resolution. Upper pane shows the matter power spectra for the symmetron model $1_{\mathbb{C}}$, with the middle pane given the relative difference with respect to the $N = 1280^3$ simulation. The lower pane shows the relative difference in the analogue case but for Λ CDM simulation.

B Convergence

We present here a convergence analysis to indicate that the general results we are seeing come from the physical model, which is being solved with appropriate temporal and spatial resolution. We are, however, still seeing some errors on selected quantities which we discuss the significance and cause of.

In Fig. 16, we show the spatial convergence in the matter power spectrum for model 1 (top and

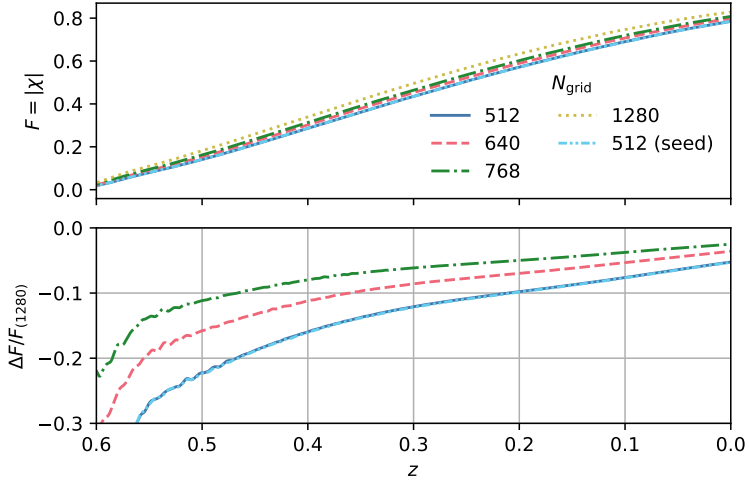


Figure 17: Convergence of box averaged norm of the scalar field $|\chi| = \sqrt{\chi^\dagger \chi}$ for the model 1_C at different spatial resolutions. ‘seed’ indicates that the simulation is run with a different seed number.

middle panels) and Λ CDM (bottom panel). We see convergence in both cases, though faster for the Λ CDM case. For example, the error on $k = 2 h \text{ Mpc}^{-1}$ for $N = 512^3$ increases by a factor ~ 1.4 for the symmetron case, with respect to Λ CDM. Since the realisation is not the same at different spatial resolutions, we are seeing the effect of sample variance at small k .

Figure 17 shows the time evolution of the volume averaged norm of the scalar field $\sqrt{\chi^\dagger \chi}$. The exact time of start of the phase transition is very sensitive to the resolution, allowing a slightly earlier phase transition in the more highly resolved case, causing a slight horizontal displacement, approaching a 5% error towards the present time, which improves with higher resolution. We note that sample variance is not important here, as the different seed number has no effect. Although the relative error is decreasing, we see an almost constant absolute error after $z \sim 0.5$, owing to the time displacement of the different resolution simulations.

Finally, in Fig. 18, we check for errors on the observed string density in the box. The relevant quantity that would be expected to be consistent in fully resolved simulations is the string energy density, ρ_{string} , which relates to the fraction of lattice points occupied by strings, F , as

$$\rho_{\text{string}} = F \mu / dx^2, \quad (\text{B.1})$$

where dx is the spatial resolution of the simulation and $\mu \equiv \int_0^{2\pi} d\theta \int_{-\infty}^{\infty} r dr V(\phi)$ is the string tension. In particular on this convergence check, we notice a significant impact of changing the seed number of the simulation; see the left panels. This indicates that the error might be dominated by sample variance, since the box volume is only forming a few strings in model 1_C , which we see to be the case in Fig. 3. Since we do not have concordance between phase realisation at the different spatial resolutions, in effect, every resolution level has a slightly different number of strings, and different number of string annihilations and interactions. This indicates that model 1_C errors might improve on simulating a larger volume or different parameters with smaller string spacings. However, the error we see is still less than $\sim 25\%$, apart from in the very early stages of the phase transition. In the right panels of Fig. 18, we see that decreasing the Compton wavelength, which we know reduces the string separation (see Fig. 3), or increasing the volume while keeping resolution constant, reduces the effect of sample variance on from $\sim 30\%$ to 5-10%. The height of the initial plateau immediately after the phase transition varies with spatial resolution, as shown in the upper left panel of Fig. 18. At early times, defect formation is characterised by small field amplitudes and spurious phase discontinuities

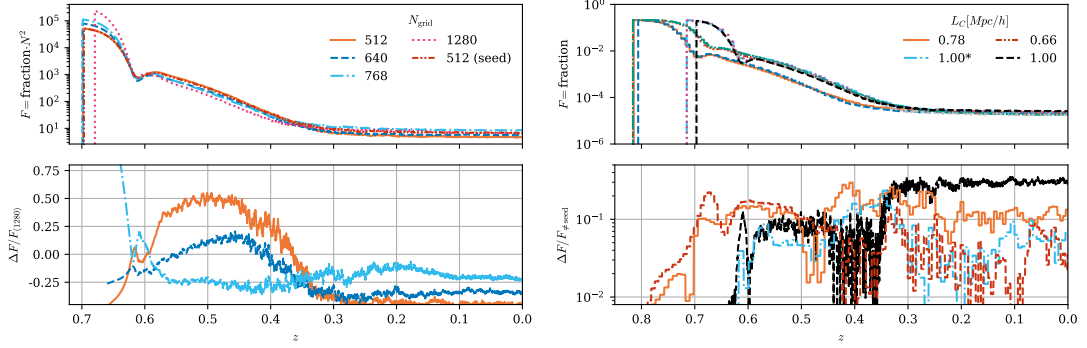


Figure 18: Fraction of volume of simulation occupied by strings. Left panel: The case of model 1_C , with z_* , β , $L_C = 0.91, 16, 1 h^{-1} \text{Mpc}$. Box fraction is multiplied N_{grid}^2 for correct scaling of 1-dimensional objects. Right panel: Comparison for pairwise simulations with different seed numbers, for differently chosen Compton wavelengths, indicating the effect of sample variance. Asterisk on green graph label indicates that the pair is done in a larger box $B = 750 h^{-1} \text{Mpc}$.

identified by the defect finder, which later merge into coherent structures. These initial plateaus can be made to overlap by removing the N^2 factor, which assumes that physical strings are one-dimensional objects and therefore scale as $F \sim N^{-2}$. This indicates that the initial defects are instead formed as three-dimensional collapsing regions in underdensities, which subsequently evolve into extended one-dimensional strings. These three-dimensional collapse regions are therefore resolved with a different scaling behaviour.

In conclusion, spectra and background quantities are found to have little effect from sample variance and are both converging with spatial resolution. The initially large but decreasing error of background quantities are likely caused by sensitivity of the time of the start of the phase transition on the spatial resolution, as underdensities are available earlier in the more finely resolved simulations. The string energy density is resolved, assumedly up until sample variance, which is found to be decreasing with more ergodic samples. For quantities that may be sensitive to string density, such as gravitational wave amplitudes (when dominated by defect emission), there might be a corresponding error of 5-30%, depending on the sample choice. This sensitivity is, as expected, higher than in the case of domain walls [23, 41], which cover more of the simulation volume. The error will improve by increasing the dynamical range of the simulations.

C Performance

The main simulations were run on the Eiger supercomputer at the Swiss National Supercomputing Centre (CSCS) using 50 nodes of $2 \times \text{AMD 7742}$ chips, giving a total of 6400 cores. The simulation domain was decomposed into 80×80 rods. We observe the runtime costs as

$$\phi \in \mathbb{C} : 30.6 \times 10^3 \times \left(0.41 + 0.59 \times \frac{0.07}{C(\phi)}\right) \left(\frac{N}{1280}\right)^4 \times \left(\frac{1}{C(\text{cdm})}\right) \text{CPU-h}, \quad (\text{C.1})$$

$$\phi \in \mathbb{R} : 32.2 \times 10^3 \times \left(0.39 + 0.61 \times \frac{0.07}{C(\phi)}\right) \left(\frac{N}{1280}\right)^4 \times \left(\frac{1}{C(\text{cdm})}\right) \text{CPU-h}, \quad (\text{C.2})$$

plus the output cost, which was an additional 10% for the output produced in this case, of which the main expense was the I/O related to animations and snapshots. We have conservatively assumed a N^4 scaling, as the run time is dominated by lattice updates $\propto N^3$ and we assume a constant Courant factor – $C(\text{cdm})$ and $C(\phi)$ for CDM and the scalar field, respectively – which means that the number

of time steps is $\propto N$. We see a more or less similar performance between the $\phi \in \mathbb{C}, \mathbb{R}$ cases. The case of Λ CDM can be recovered for $C^{(\phi)} \rightarrow \infty$. 90% of the scalar field sector's runtime is coming from the field equations solver, which makes it the best candidate for optimisations. Possible improvements might be offered by applying implicit solvers instead of the 4th order Runge-Kutta solver currently used, although the relevant physical scales should be considered carefully, see [23]. This sort of physics problem, requiring a large number of timesteps for the rapidly oscillating scalar, will in particular benefit from working on GPUs, which is the subject of a future work.